Water Resources Research

RESEARCH ARTICLE
10.1029/2023WR034948

Key Points:

- StorAge Selection-based water age modeling revealed a strong preference for young water and an inverse storage effect during tile discharge generation
- Nitrate export regime was modulated by an interplay between water mixing, flow path activation, and the vertical distribution of soil nitrate
- Combining water age modeling with nitrate isotope analysis has the potential to improve the modeling of reactive nitrate transport

Supporting Information:

Supporting Information may be found in the online version of this article.

Correspondence to:

Z. Yu,
zjyu@illinois.edu

Citation:

Yu, Z., Hu, Y., Gentry, L. E., Yang, W. H., Margenot, A. J., Guan, K., et al. (2023). Linking water age, nitrate export regime, and nitrate isotope biogeochemistry in a tile-drained agricultural field. *Water Resources Research*, *59*, e2023WR034948. https://doi.org/10.1029/2023WR034948

Received 22 MAR 2023
Accepted 25 NOV 2023

Linking Water Age, Nitrate Export Regime, and Nitrate Isotope Biogeochemistry in a Tile-Drained Agricultural Field

Zhongjie Yu[1], Yinchao Hu[1], Lowell E. Gentry[1], Wendy H. Yang[2,3], Andrew J. Margenot[4], Kaiyu Guan[1,5], Corey A. Mitchell[1], and Minpeng Hu[1]

[1]Department of Natural Resources and Environmental Sciences, University of Illinois at Urbana-Champaign, Urbana, IL, USA, [2]Department of Plant Biology, University of Illinois at Urbana-Champaign, Urbana, IL, USA, [3]Department of Earth Science & Environmental Change, University of Illinois at Urbana-Champaign, Urbana, IL, USA, [4]Department of Crop Sciences, University of Illinois at Urbana-Champaign, Urbana, IL, USA, [5]Agroecosystem Sustainability Center, University of Illinois at Urbana-Champaign, Urbana, IL, USA

Abstract Accurately quantifying and predicting the reactive transport of nitrate (NO_3^-) in hydrologic systems continues to be a challenge, due to the complex hydrological and biogeochemical interactions that underlie this transport. Recent advances related to time-variant water age have led to a new method that probes water mixing and selection behaviors using StorAge Selection (SAS) functions. In this study, SAS functions were applied to investigate storage, water selection behaviors, and NO_3^- export regimes in a tile-drained corn-soybean field. The natural abundance stable nitrogen and oxygen isotopes of tile drainage NO_3^- were also measured to provide constraints on biogeochemical NO_3^- transformations. The SAS functions, calibrated using chloride measurements at tile drain outlets, revealed a strong young water preference during tile discharge generation. The use of a time-variant SAS function for tile discharge generated unique water age dynamics that reveal an inverse storage effect driven by the activation of preferential flow paths and mechanically explain the observed variations in NO_3^- isotopes. Combining the water age estimates with NO_3^- isotope fingerprinting shed new light on NO_3^- export dynamics at the tile-drain scale, where a large mixing volume and the lack of a strong vertical contrast in NO_3^- concentration resulted in chemostatic export regimes. For the first time, NO_3^- isotopes were embedded into a water age-based transport model to model reactive NO_3^- transport under transient conditions. The results of this modeling study provided a proof-of-concept for the potential of coupling water age modeling with NO_3^- isotope analysis to elucidate the mechanisms driving reactive NO_3^- transport.

Plain Language Summary Accurately quantifying the transport and transformation of NO_3^- in hydrologic systems continues to be a challenging task. In this study, we combined water age modeling with NO_3^- isotope analysis to understand how hydrological processes, microbial reactions, and management practices interact to control NO_3^- loss from a tile-drained agricultural field. While water age is an important descriptor of how water flows through hydrologic systems, NO_3^- isotopes contain unique information about NO_3^- sources and microbial reactions that produce, consume, and recycle NO_3^- during hydrologic transport. Therefore, the coupled use of water age modeling and NO_3^- isotopes provides complementary information about water flow and microbial NO_3^- cycling. Results from this study show that tile discharge was fed by younger stored water flowing through big soil pores when the tile drained system was wet. Based on the measured NO_3^- isotopes, we were able to discern key microbial NO_3^- cycling reactions that occurred during the transport of NO_3^- with water, which, in turn, provided important evidence to confirm the dominant mechanism that controls how water flows at the tile-drain scale. Our finding suggests that combining water age modeling with NO_3^- isotopes is a promising way forward for modeling coupled water and NO_3^- transport.

1. Introduction

The transit time of water is a fundamental descriptor of hydrologic systems (McGuire & McDonnell, 2006). Recent advances in our capability to model time-variant water transit times have substantially improved our understanding of storage, flow paths, and source of water in complex watersheds (Botter et al., 2011; Harman, 2015; Rinaldo et al., 2015; van der Velde et al., 2012). The differentiated concepts of celerity controlling rainfall-runoff responses and velocity driving water particle movement are increasingly recognized and used to guide watershed studies that aim to reconcile the diverse controls on solute transport (Benettin et al., 2020; Hrachowitz et al., 2015; Van der Velde, De Rooij, et al., 2010). However, applications of the newly evolved water age theory to interpret reactive solute dynamics remain rare in the literature, precluding generalization of findings across temporal, spatial, and physiographical scales. Moreover, as concluded by several recent synthesis studies (Benettin et al., 2022; Hrachowitz et al., 2016; Li et al., 2021), a unified modeling framework based on water age theory for coupled water and reactive solute transport remains out of reach. This is mainly due to the continued challenge in resolving the large variability of water mixing and selection behaviors at the watershed scale (Benettin et al., 2022), as well as an incomplete understanding of the nonlinear interactions between hydrological and biogeochemical processes that govern solute dynamics along hydrologic flow transport (Li et al., 2021). Overcoming these emergent challenges is imperative for modeling the transport and cycling of nitrate (NO_3^-) at watershed scales and beyond, where model simulations and predictions are often confronted by the heterogeneous distribution of NO_3^- sources and the uncertain occurrence and magnitude of NO_3^- transformation processes (Kumar et al., 2020).

The natural abundance stable nitrogen (N) and oxygen (O) isotopes of NO_3^- (hereafter referred simply as to NO_3^- isotopes) have long been used as a tracer of NO_3^- in hydrologic systems (Kendall et al., 2007). The unique power of NO_3^- isotopes stems from the distinct partitioning of N and O isotopes between chemical species or phases, known as isotope fractionation (see Section 2.2 for more details). Previous studies at the watershed scale have combined NO_3^- isotope measurements with end-member mixing (e.g., Kaushal et al. (2011), Yi et al. (2017), and Sebestyen et al. (2019)) and mass balance models (e.g., Houlton et al. (2006), Houlton and Bai (2009), and Fang et al. (2015)) to differentiate N sources, track their distributions, and determine the extent of biogeochemical transformations acting on NO_3^-. However, previous applications of NO_3^- isotopes at the watershed scale typically did not explicitly account for the variability of NO_3^- isotopic source signatures resulting from fractionation processes, or relied heavily upon assumptions of steady state or system stationarity, which are often violated under transient transport conditions. To our knowledge, the utility of NO_3^- isotopes has not been rigorously evaluated against complex hydrologic conditions beyond the binary classification of base versus storm flows. To that end, combining NO_3^- isotope measurements with the formulation of transport by time-variant water age distributions may better contextualize observed NO_3^- isotopic variations, thus providing a new opportunity to dissect the often intertwined hydrological and biogeochemical processes that control reactive NO_3^- transport.

In this proof-of-concept study, we combined the recently developed StorAge Selection (SAS) functions for water age modeling with NO_3^- isotope measurements to examine coupled water and NO_3^- transport in a tile-drained agricultural field in east-central Illinois, USA. A substantial fraction of agricultural land in the Upper Midwest U.S. is tile-drained to maintain high crop production by increasing soil drainage (Blann et al., 2009). The installation of subsurface drainage tiles has caused profound alterations in water and solute transport in this region, including intensified hydrographs, shortened groundwater flow paths, and loss of nutrients and agrochemicals via tile discharge (see Blann et al. (2009) and references cited therein). Indeed, the combination of N fertilizer applications on tile-drained watersheds has been considered the dominant source of riverine NO_3^- yields in the upper Mississippi River Basin (David et al., 2010; Ma et al., 2023). Nevertheless, it remains elusive how hydrological, biogeochemical, and management factors interact to control water and NO_3^- transport in tile-drained systems. For example, recent studies revealed a threshold behavior in tile discharge generation, suggesting that any deficits in below-tile storage must be filled to raise the groundwater table to the tile elevation before significant tile discharge can be generated (Cain et al., 2022; Williams & McAfee, 2021). The remaining questions to be answered are what sources of water mainly contribute to tile discharge and how these contributions vary with antecedent wetness conditions. In addition, variations in NO_3^- load from many tile-drained fields are found to be predominantly driven by the duration and quantity of tile discharge (Bauwe et al., 2020). In the watershed solute transport literature, this stationary export regime, termed "chemostasis," has been variously hypothesized to result from a proportional change in flow- and solute-generating areas (Godsey et al., 2009), or vertical (Seibert et al., 2009; Thompson et al., 2011) and areal (Basu et al., 2010) homogeneous distribution of solute stores. However, while all these hypotheses allude to an intimate link between solute export regimes and water age dynamics (Musolff et al., 2017), we still lack robust observational constraints that can guide the testing of these hypotheses by disentangling coupled water and reactive solute transport.

Here we hypothesized that water age, NO_3^- export, and NO_3^- isotope dynamics are inherently linked in tile-drained agricultural systems. To test this hypothesis, we focused on discharge, solute concentrations (i.e., chloride (Cl) and NO_3^-), and NO_3^- isotopes measured directly from tile drain outlets to isolate dominant water and solute transport mechanisms operating at this scale. Specifically, we addressed three key questions in this study: (a) How does the age of tile discharge vary with hydroclimatic conditions and reflect activation of distinct flow paths? (b) how does tile NO_3^- export respond to variations in tile water age? and (c) What added value can NO_3^- isotope measurements provide in terms of modeling coupled water and NO_3^- transport? Finally, based on results from this study, we discussed implications for modeling NO_3^- transport at the watershed scale and management of tile-drained fields.

2. Background Theory

Here we provide a brief summary of recent advances in modeling water age distributions and NO_3^- isotope fingerprinting techniques. The goal is not to provide a comprehensive review on these subjects, which can be found elsewhere (e.g., Rinaldo et al. (2015), Hrachowitz et al. (2016), Benettin et al. (2022), Böhlke (2002), Kendall et al. (2007), and Casciotti (2016)). Instead, through this summary, we hope to provide a necessary context that will ease the description of our modeling method and the interpretation of tracer data obtained in this study.

2.1. Water Age Distributions and SAS Functions

The water age concept is based on the representation of hydrologic systems as a dynamic population of water particles that age as they move from inflow (e.g., precipitation) to outflow (e.g., discharge and evapotranspiration). More specifically, by conceptualizing a hydrologic system as a single control volume with a total storage (S), an influx of precipitation (J) as the only water input, and discharge (Q) and evapotranspiration (ET) as outputs, the water age (T) is defined as the time interval between the entrance of a water particle into the volume and its exit via either Q or ET. Based on this definition, the T is conditioned on the exit time. The water age distribution (p), therefore, summarizes the distribution of T for a cohort of such particles, reflecting the random nature of T as a result of complex dispersion in the subsurface. Importantly, the age distributions of outfluxes (p_Q and p_{ET}) are distinct from the storage age distribution (p_S), which refers to the distribution of the time elapsed since the entrance of a water particle that is still present within the storage.

In real-world hydrologic systems, the age distributions of storage and outfluxes are variable in time due to the nonstationary entrance of zero-age particles via J and the nonuniform selection of older particles by Q and ET (Botter et al., 2011; Harman, 2015; van der Velde et al., 2012). The temporal evolution of the water age distributions can be formally described by the master equation expressing mass conservation over time and age (Botter et al., 2011), which has been reformulated by Harman (2015) using the cumulative age distributions as:

$$\frac{\partial S_T(T,t)}{\partial t} = J(t) - Q(t)P_Q(T,t) - \mathrm{ET}(t)P_{\mathrm{ET}}(T,t) - \frac{\partial S_T(T,t)}{\partial T} \tag{1}$$

where t is time; $P_Q(T, t)$ and $P_{\mathrm{ET}}(T, t)$ are the cumulative age distributions for Q and ET, respectively; and $S_T(T, t)$ is age-ranked storage (Harman, 2015; van der Velde et al., 2012), defined as the product of the cumulative storage age distribution, $P_S(T, t)$, and the storage at time t:

$$S_T(T,t) = S(t)P_S(T,t) \tag{2}$$

Thus, the age-ranked storage $S_T(T, t)$ quantifies the cumulative volumes of water in storage as classified according to their age T at time t (Harman, 2015). The introduction of S_T makes it possible to re-express $P_Q(T, t)$ and $P_{\mathrm{ET}}(T, t)$ by assigning each of them a SAS function $\Omega(S_{T,}\ t)$ that dictates how much each different age-ranked storage contributes to Q and ET:

$$\Omega_Q(S_T(T,t),t) = P_Q(T,t) \tag{3}$$

$$\Omega_{\mathrm{ET}}(S_T(T,t),t) = P_{\mathrm{ET}}(T,t) \tag{4}$$

This re-expression greatly simplifies the parameterization of $P_Q(T, t)$ and $P_{\mathrm{ET}}(T, t)$, which can be otherwise challenging because $P_Q(T, t)$ and $P_{\mathrm{ET}}(T, t)$ are dependent on the entire history of storage states. In addition, solution to Equation 1 allows one to back-calculate, at any time, the storage age distribution $p_S(T, t)$ and through, the SAS functions, the outflux age distributions, $p_Q(T, t)$ and $p_{\mathrm{ET}}(T, t)$:

$$p_s(T,t) = \frac{\partial P_s(T,t)}{\partial T} = \frac{\partial S_T(T,t)}{\partial T}\frac{1}{S(t)} \tag{5}$$

$$p_Q(T,t) = \frac{\partial P_Q(T,t)}{\partial T} = \frac{\partial \Omega_Q(S_T(T,t),t)}{\partial T} \tag{6}$$

$$p_{\mathrm{ET}}(T,t) = \frac{\partial P_{\mathrm{ET}}(T,t)}{\partial T} = \frac{\partial \Omega_{\mathrm{ET}}(S_T(T,t),t)}{\partial T} \tag{7}$$

The SAS approach can be used to simulate movement of tracers such as Cl and stable water isotopes through a hydrologic system, which in turn allows inverse modeling of the shape and variability of SAS functions using tracer data. Although tracers like Cl often do not behave conservatively due to mass transfer, evaporation, and/or biogeochemical processes (Kirchner et al., 2010), these nonconservative behaviors can be accounted for under the SAS modeling framework using a generalized expression of solute transport (Harman, 2015; van der Velde et al., 2012):

$$C_Q(t) = \int_0^\infty C_S(T,t)p_Q(T,t)dT \tag{8}$$

Equation 8 states that each stored volume can be associated with a tracer concentration $C_S(T, t)$, which retains impacts from all related input and nonconservative transport processes. The tracer concentration in Q, $C_Q(t)$, is therefore obtained by integrating the weighted contribution of all discharged volumes according to $p_Q(T, t)$.

Previous applications of SAS functions to characterizing time-variant water age distributions have provided insight into water mixing and selection mechanisms in various hydrologic settings. At the watershed scale, the shape of SAS functions for Q has often been found to reflect marked preference for younger stored water. Moreover, this preferential release of younger water is also often more pronounced during wetter conditions or larger storms—a phenomenon known as the “inverse storage effect” (Harman, 2015). Consequently, a larger storage promotes an increase in younger water release, resulting in shorter transit times (Benettin et al., 2022). The physical origin of the inverse storage effect has been linked to activations of fast/short flow paths triggered by exceedance of certain storage thresholds (Kaandorp et al., 2018; Kim et al., 2016; Pangle et al., 2017; Wilusz et al., 2020; Yang et al., 2018). However, on the other hand, deviations of water age dynamics from a young water preference and inverse storage effect have also been reported in some watersheds, where increased hydrologic connectivity of aged water in storage may cause mobilization of these water during storm events (Klaus et al., 2013), and for vertical water percolation in soils, where flow regime was dominated by advection (Asadollahi et al., 2020; Queloz et al., 2015). These findings advocate for more research on the variability of water age dynamics across diverse hydrologic compartments. In addition, because the estimation of SAS functions relies on calibration against tracer data, definitive diagnosis of an inverse storage effect can be challenging due to nonconservative tracer behaviors and uncertainties in SAS model inputs and model structure (Harman, 2015).

2.2. Nitrate Isotope Fingerprinting

Just as stable water isotopes are to characterizing water mixing and flow dynamics in hydrologic systems, stable isotope ratio measurements of NO_3^- are an indispensable tool for understanding the dynamics and relative rates of biogeochemical processes comprising the N cycle (Böhlke, 2002; Casciotti, 2016; Kendall et al., 2007). N and O isotope ratios are generally expressed using the delta (δ) notation in units of per mil (‰):

$$\delta^{15}\mathrm{N} = \left({}^{15}\mathrm{N} : {}^{14}\mathrm{N}_{\mathrm{sample}} / {}^{15}\mathrm{N} : {}^{14}\mathrm{N}_{\mathrm{reference}} - 1\right) \times 1000 \tag{9}$$

$$\delta^{18}\mathrm{O} = \left({}^{18}\mathrm{O} : {}^{16}\mathrm{O}_{\mathrm{sample}} / {}^{18}\mathrm{O} : {}^{16}\mathrm{O}_{\mathrm{reference}} - 1\right) \times 1000 \tag{10}$$

N_2 in air is the N isotope reference, and O in Vienna standard mean ocean water (VSMOW) is the O isotope reference.

The $\delta^{15}N$ and $\delta^{18}O$ values of NO_3^- vary during enzyme-driven biological processes, which are arguably most relevant in the context of NO_3^- cycling in hydrologic systems (Kendall et al., 2007). Specifically, enzymatic isotope fractionation arises from small differences in the rates of reactions containing heavy and light isotopes. If the reaction rate can be characterized by a first-order dependence on the substrate concentration, then the fractionation factor, α, can be defined as ${}^{\mathrm{L}}k/{}^{\mathrm{H}}k$, where ${}^{\mathrm{L}}k$ is the first-order rate constant for the reaction of the light isotope-containing molecule (e.g., ${}^{14}N^{16}O^{16}O^{16}O$) and ${}^{\mathrm{H}}k$ is the first-order rate constant for the reaction of the heavy isotope-containing molecule (e.g., $^{14}N^{18}O^{16}O^{16}O$) (Bigeleisen & Wolfsberg, 1957). The fractionation factor can also be expressed in per mil as an isotope effect, ε, defined as:

$$\varepsilon = (\alpha - 1) \times 1000 = ({}^{L}k / {}^{H}k - 1) \times 1000 \tag{11}$$

Most of enzymatic reactions involved in biogeochemical NO_3^- cycling preferentially use light isotope-containing molecules due to a larger energy investment for using the heavier isotope (Granger & Wankel, 2016). This preference at the enzyme level results in an enrichment of heavy isotopes in the substrate pool (correspondingly an enrichment of light isotopes in the product pool) and is termed the kinetic isotope effect, with $\alpha > 1$ and $\varepsilon > 0$ (because ${}^{L}k/{}^{H}k > 1$).

Recent progress in the quantification of kinetic isotope effects for key microbial processes of the N cycle has provided a basis for interpreting the $\delta^{15}N$ and $\delta^{18}O$ values of environmental NO_3^- (Granger & Wankel, 2016; Yu & Elliott, 2018). For example, nitrification (i.e., aerobic oxidation of ammonia (NH_3) to NO_3^-) has been shown to express a strong kinetic N isotope effect, with reported $^{15}\varepsilon$ ranging between 25 and 35‰ (Casciotti et al., 2003; Mariotti et al., 1981; Yu & Elliott, 2018). This means that when NH_3 supply to nitrifying microbes is not limited and the kinetic isotope effect is fully expressed, the NO_3^- produced has a $\delta^{15}N$ value about 30‰ lower than that of the substrate NH_3. The isotope systematics underlying the $\delta^{18}O$ of NO_3^- produced from nitrification is more complex, as it involves kinetic O isotope fractionations during the incorporation of O atoms from water and O_2 into the produced NO_3^- as well as O isotope exchange between water and nitrite, an intermediate of nitrification (Buchwald & Casciotti, 2010; Casciotti et al., 2010). Collectively, these O isotope fractionations form a direct link between the $\delta^{18}O$ of water and that of NO_3^- resulting from nitrification in soil (Yu & Elliott, 2018).

Perhaps the most powerful utility of NO_3^- isotopes in hydrologic systems is to trace denitrification. While assimilatory NO_3^- uptake by plants and microbes (Fang et al., 2015) and physical processes like diffusion and dispersion (Mnich & Houlton, 2016) do not exhibit appreciable isotope fractionations on NO_3^-, enzymatic bond breaking during denitrification imprints a strong isotope effect on NO_3^- isotopes (Denk et al., 2017; Yu & Elliott, 2021). As a result, denitrification causes the $\delta^{15}N$ and $\delta^{18}O$ values of the residual NO_3^- to increase exponentially as NO_3^- concentrations decrease. More importantly, the effects of denitrification on the dual isotopic composition of NO_3^- are considered coupled since both the N and O atoms originate in the same molecule. This coupled fractionation is analogous to the simultaneous enrichments of heavier hydrogen and O isotopes in the residual water during evaporation (Bowen et al., 2018), and is represented by a line with a slope of 1 in the dual isotope space of NO_3^- (Granger et al., 2006), analogous to the evaporation line in the dual isotope space of water. Therefore, deviations from the denitrification line may indicate occurrence of NO_3^- production processes such as nitrification and/or changes in the $\delta^{15}N$ and $\delta^{18}O$ values of the source NO_3^- (Granger & Wankel, 2016).

3. Materials and Methods

3.1. Study Site

This study was conducted on a tile-drained field in Douglas County located in the Upper Embarras River (UER) watershed near Tuscola, Illinois (39°43′ N, 88°14′ W) (Figure 1a). The field is about 60 ha total and constitutes two adjacent sub-fields separated by a ditch that empties into the UER approximately 6 km distant (Figure 1a). This region has a humid continental climate, with cold winters (average January temperature of −2°C) and warm summers (average July temperature of 23°C). The 30-year (1993–2022) mean annual precipitation was 1,008 mm (NOAA, 2022). Minor snow accumulation is not uncommon in winter at this site, but it rarely lasts longer than a few weeks, and on average melts within a few days. Throughout the study period (2015–2022), weather conditions at the site, including precipitation, air temperature, humidity, solar radiation, and wind speed, were measured at 15-min intervals using a weather station equipped with a tipping bucket rain gauge (Davis Instruments Corporation, USA) (Figure 1a). Snowfall data measured in liquid water equivalents were retrieved from a meteorological station about 9 km from the site (NOAA, 2022).

The UER watershed is representative of the glaciated Midwest, characterized by low-gradient topography and poorly drained soils. The study site is nearly flat with land surface slopes ranging from 0% to 2%. Soil profiles at the site reflect glacial deposition patterns, with very deep, fine-textured soils formed on lacustrine deposits, and bedrock depths are believed to be 50–100 m below the surface (Andino et al., 2020; Cain et al., 2022). The soil at the site is classified as a Milford silty clay loam (fine, mixed, superactive, mesic Typic Endoaquolls) (USDA-NRCS, 2016).

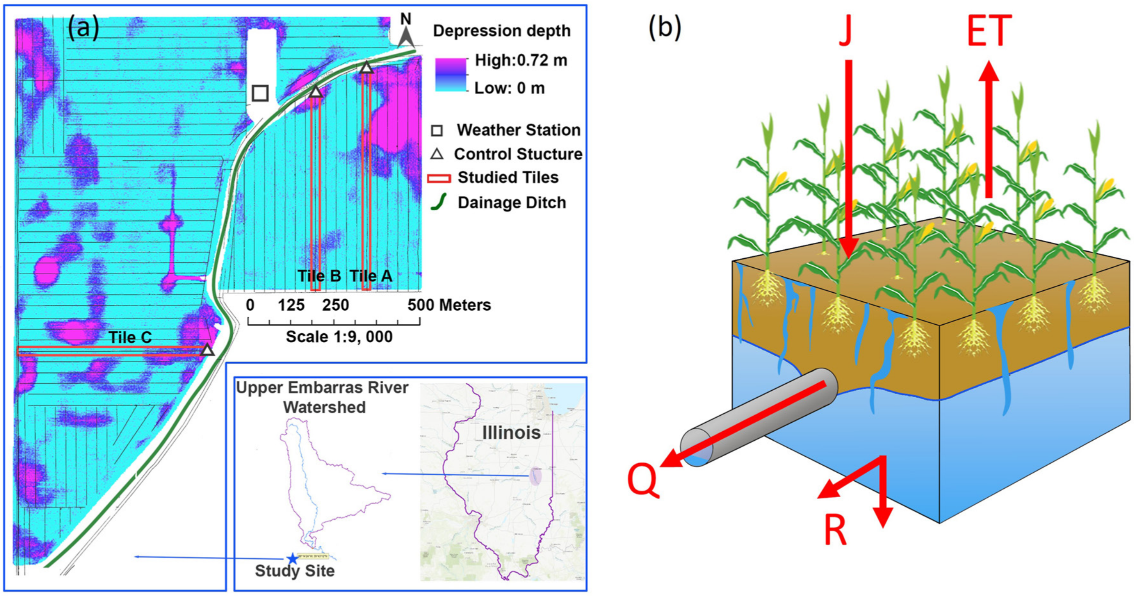

Figure 1. (a) Study location and study site map showing the parallel tile drain systems and depression depth derived from 1.8-m LiDAR digital elevation data of the site. (b) Schematic of the control volume used in the StorAge Selection modeling. J, ET, *Q*, and R denote precipitation, evapotranspiration, tile discharge, and a combined flux of deep percolation and groundwater exfiltration, respectively.

For each of the two sub-fields comprising the study site, a system of parallel drains was installed approximately 40 years ago at depths ranging from 1.2 to 1.5 m below the soil surface. Each drain system is composed of one main drain fed by a set of lateral drains spaced 30.5 m apart, all consisting of 12.7 cm diameter perforated plastic pipe. The drain outlet of each sub-field empties into the ditch 1.5 m above the ditch bed. During the study period, each of the lateral tiles in the two sub-fields was monitored as a part of a replicated fertilizer management study (Andino et al., 2020). Specifically, an inline water level control structure (AgriDrain Corporation, USA) was installed on each lateral tile at approximately 4 m from the junction with the tile main for discharge and solute concentration measurements.

This study focuses on the field-scale observations on three lateral tiles, hereafter referred to as Tiles A, B, and C (see their locations in Figure 1a). The lengths of these tiles range from 500 to 570 m. Assuming that the midpoints between two adjacent tiles form a no-flow boundary, the discharge-contributing area of the three tiles were estimated to range from 1.6 to 1.8 ha. Compared to Tile B, Tile A and Tile C are bounded by more depressional areas, although the areas intersected were limited and spatially scattered (Figure 1a).

Identical agricultural management practices were applied to the soil overlying the three tiles. Briefly, a 2-year crop rotation of corn-soybean, a common practice in the Midwestern U.S., was used. During the study period, corn was planted in 2015, 2017, 2019, and 2021, and soybean was planted in alternative years of 2016, 2018, 2020, and 2022. While soybean was no-till planted, strip-till was used during the fall prior to the corn phase for seedbed preparation. In the corn years, anhydrous NH_3 was knifed into surface soil in the spring before corn planting, and 32% urea-ammonium-nitrate (UAN) was side-dressed after corn emergence. N fertilizer was not applied to soybean. During the study period, potash (KCl) was applied once to the entire field on 17 April 2021 as a potassium fertilizer. The application rate was 50 kg Cl ha^{-1}. The field is not irrigated, so the only water input is precipitation.

3.2. Tile Drainage Measurements and Concentration Data

Each inline monitoring structure was equipped with a stoplog containing a 45° V-notch weir, and water depth within the structure was recorded using a water level sensor (Model 3001, Solinst, USA) at 15-min intervals. Tile discharge rates were determined using a discharge equation for inline water level control structures developed by Chun and Cooke (2008) and normalized by the estimated tile drainage area of the respective tiles. Daily discharge rates were then aggregated from the 15-min data. From January 2015 to July 2022, we collected water samples

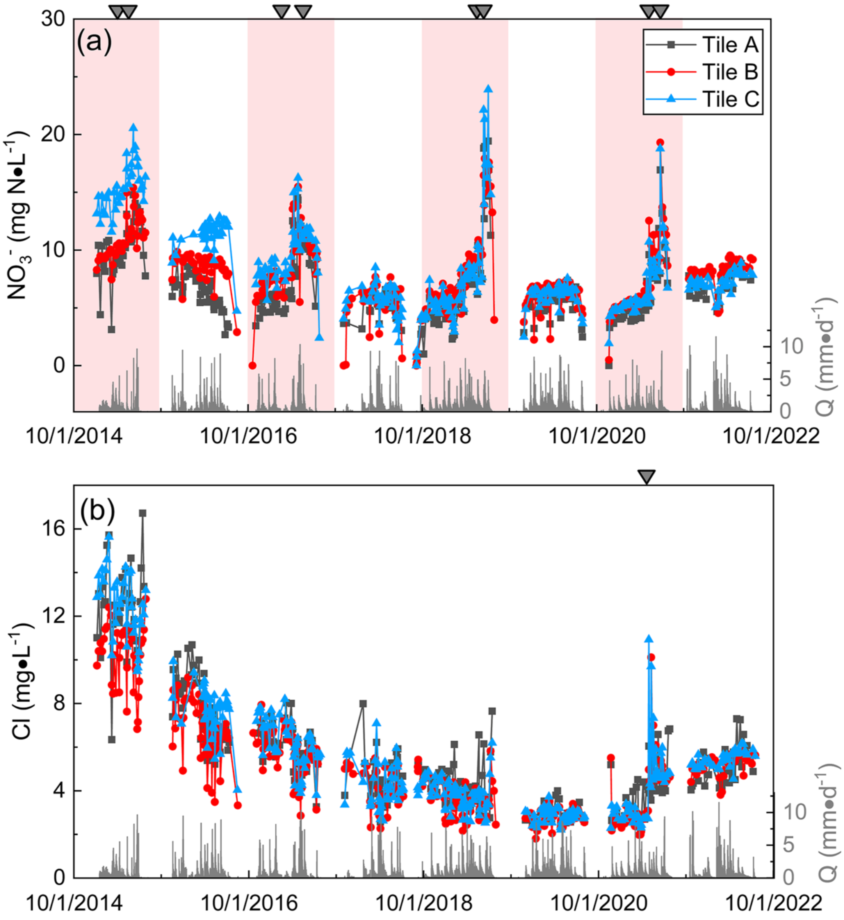

Figure 2. Temporal variations in (a) NO_3^- and (b) Cl concentrations at the three tiles. Pink faded boxes in panel (a) indicate corn years. Gray triangles at the top axis indicate the timing of N and potash fertilizer applications. Tile discharge measured at Tile B is shown for comparison with the concentration data.

from each of the three inline monitoring structures using automated samplers (ISCO 3700C, Teledyne Isco Inc., USA). The sampling frequency was weekly. Water samples ($n = 1090$) were retrieved from the automated water samplers within 48 hr of the collection. Upon return to the laboratory, water samples were vacuum filtered and analyzed for NO_3^- and Cl concentrations using a Dionex ICS1600 Ion Chromatograph.

To facilitate the modeling of water age and the related analysis for NO_3^- export regime, the measured NO_3^- and Cl concentrations for all three tiles along with tile discharge measured at Tile B are shown in Figure 2. Every year during the study period, the tiles ceased to flow at the onset of peak growing season (GS) (i.e., late July to early August) due to enhanced crop ET. Typically, not long after crop harvest in October or November, the flow resumed, usually triggered by a few intense precipitation events. Here, we use water year, defined as 1 October to 30 September, instead of calendar year, to describe the measured flow and tracer results, because it better aligns with the onset and cessation of the tile discharge. The measured NO_3^- concentrations exhibit high temporal variability during the corn years, with abruptly increased concentrations following every fertilization event (Figure 2a). In contrast, NO_3^- concentrations measured during the soybean years were relatively stable (Figure 2a). These patterns were consistent among the three tiles.

A unique trend emerged from the measured Cl concentrations (Figure 2b). The Cl concentrations decreased gradually from about 10 to 16 mg L^{-1} at the beginning of the study period to less than 4 mg L^{-1} in the spring of 2021, and then increased to high values again following the potash application (Figure 2b), the first application since the study initiated in 2015. Therefore, the initial high Cl concentrations in discharge were due to past potash fertilizer applications that occurred prior to the onset of this study. Though we do not know exact dates and input amounts, these pre-study Cl inputs via potash fertilizer are likely to be of similar or greater magnitude given agronomic recommendations of adding 224 kg ha^{-1} potash (90 kg Cl ha^{-1}) every 2–4 years (Illinois Agronomy Handbook, 2014). Furthermore, at shorter time scales, the Cl concentrations fluctuated considerably in response to flow events. Combined, these patterns depict a diluting system, where legacy stores of Cl undergo a gradual reduction due to continued flushing by Cl-less precipitation water. Indeed, long-term observations of wet deposition at a nearby National Atmospheric Deposition Program site (Bonville, Illinois; site ID IL11) confirmed negligible Cl content in rainwater (<0.1 mg L^{-1}) during the study period (NADP, 2023).

3.3. Nitrate Export Regime Categorization

To characterize NO_3^- export regime, the measured NO_3^- concentrations were pooled from all three tiles and then compared to the corresponding tile discharge. For this analysis, we classified the NO_3^- and discharge data by crop year (i.e., water year with corn or soybean being cultivated), and further divided the corn data into growing and nongrowing seasons based on the timing of spring pre-plant N fertilizer application. Therefore, the NGS of corn spans from the dormant period of a water year until the spring fertilizer application. This classification by crop season is operationally defined and aims to examine the management controls on NO_3^- export regimes. All concentration and discharge data for each crop season were log-transformed, and the linear slope (b) of the log-log regression of concentration and discharge was used to categorize NO_3^- export regime into flushing ($b > 0$), dilution ($b < 0$), and those showing either chemostatic or non-linear chemodynamic ($b \approx 0$) patterns (Godsey et al., 2009; Rose & Karwan, 2021). Chemostatic and non-chemodynamic patterns were differentiated based on the ratio of the coefficients of variation of concentration and discharge (CV_C/CV_Q), with $CV_C/CV_Q < 0.5$ indicating chemostatic behavior and $CV_C/CV_Q \geq 0.5$ indicating non-linear chemodynamic behavior (Musolff et al., 2015; Rose & Karwan, 2021; Thompson et al., 2011). Additionally, following Basu et al. (2010), a linear relationship between tile discharge and NO_3^- load—the product of discharge and NO_3^- concentration—was also used to detect chemostatic behavior.

3.4. Nitrate Isotopic Analysis

Water samples collected during 2021 and 2022 water years ($n = 246$) were measured for NO_3^- isotopes using the denitrifier method (Weigand et al., 2016; Yu & Elliott, 2018). Briefly, denitrifying bacteria lacking the nitrous oxide (N_2O) reductase enzyme (*Pseudomonas chlororaphos ssp. aureofaciens*) are used to convert 60 nmol of NO_3^- into gaseous N_2O. The N_2O is then purified in a series of chemical traps, cryofocused, and finally analyzed for m/z 44, 45, and 46 on a continuous flow isotope ratio mass spectrometer (Elementar Isoprime precisION, Germany). International NO_3^- reference materials USGS34 and USGS35 and an internal working standard gravimetrically prepared from USGS32 and USGS34 were used to calibrate the isotope measurements. The long-term precision for $\delta^{15}N$ and $\delta^{18}O$ determinations are ±0.1‰ and ±0.2‰, respectively.

3.5. Water Age Modeling

To estimate storage and the water age distribution of tile discharge, we simulated the transport of Cl using a modification of the open source tran-SAS model (Benettin & Bertuzzo, 2018b). The core of the model is to solve Equation 1 using the age-ranked storage and SAS functions (Equations 2–4). Detailed numerical implementation of the tran-SAS model can be found in Benettin and Bertuzzo (2018b). Below we describe the main model assumptions and modifications that are necessary to adapt the model at the tile-drain scale.

3.5.1. Boundary Conditions and Fluxes

We consider the water storage that contributes to the tile discharge and Cl mixing as a single control volume (Figure 1b). The upper boundary of the control volume is delimited by the soil surface. The subsurface lateral boundaries are defined by the midpoints between the study tiles and their adjacent tiles, consistent with the estimation of tile drainage areas. Flow across the lateral boundaries is neglected. This is a reasonable assumption given the flat topography and the high drainage density of this site that are expected to reduce hydraulic head gradients perpendicular to the lateral boundaries. We define an arbitrary lower boundary for the control volume, below which water can no longer connect to the tile drain. By this definition, the control volume can enclose a variable volume of the saturated groundwater below the tile depth, where hydraulic head differences may drive water to enter the tile drain radially from below. Based on the defined control volume, infiltrating precipitation water can leave the volume as ET to the atmosphere, flow into the tile drain (Q), deep percolation past the lower boundary, and groundwater exfiltration toward the ditch (Figure 1b). We ignored surface runoff in this study, as previous studies in this region suggested its minor importance compared to tile discharge (e.g., <10%) (Guan et al., 2011).

The combined precipitation and snowfall rates (denoted by J) and Q were used directly as inputs to the SAS model. However, quantification of the deep percolation and groundwater exfiltration fluxes is difficult because it requires detailed groundwater measurements. Without this information at hand, we lumped the two fluxes into a single flux (denoted by R) and resorted to a simple approach to estimate its average magnitude. Specifically, we compared the ratio of Q to J measured at the study site to the long-term runoff ratio of the UER watershed and attributed the difference to R. During the 8-year study period, the average Q-to-J ratios ranged between 0.27 and 0.30 for the three study tiles; the 30-year (1993–2022) average runoff ratio of the UER watershed is 0.34 (USGS, 2023). Therefore, the annual average R was estimated to be 4%–7% of the annual J, or 13%–26% of the annual Q, for the three tiles. The average R-to-Q ratio estimated this way agrees well with the finding by Van der Velde, Rozemeijer, et al. (2010), who showed via field-scale measurements that tile discharge contributed about 80% of the total discharge (i.e., the sum of overland flow, tile discharge, and groundwater exfiltration) from a lowland tile-drained field in the Netherland. To further derive a daily time series of R, we linearly scaled R with Q, so that R and Q exhibit the same temporal pattern. The rationale behind this scaling is that the flux intensities of all flow paths are closely related and ultimately controlled by groundwater table variations in lowland systems (van der Velde et al., 2009). It should be noted that by making R a unidirectional flux exiting the control volume, we necessarily ignored all related processes such as capillary rise and water infiltration from the ditch. Though a drastic simplification, this is a pragmatic approach that allowed us to estimate reasonable water age of Q using a parsimonious model.

We used the FAO approach (Allen et al., 2005) to estimate daily actual ET from the potential ET values that were estimated using the weather station data and the Penman-Monteith equation. The FAO approach uses information on crop planting date, crop growth stages, and maximum rooting depth to estimate daily ET values. The model also includes a correction factor to account for crop physiologic stress resulting from soil water deficits. Crop planting dates and growth stages in the FAO method reflected actual dates and measurements at the site. A correction factor was applied to the modeled daily ET values to close the hydrologic balance over the 8-year study period (i.e., $J = \mathrm{ET} + Q + \mathrm{R}$).

3.5.2. SAS Model Specification

Each of the outfluxes (i.e., ET, Q, and R) was assigned a SAS function to assess its impact on the storage age balance. We selected power law functions to parameterize the SAS functions because they are simple to use, yet flexible in modeling a wide range of age selection behaviors (Benettin & Bertuzzo, 2018b; Benettin et al., 2017). When using power-law SAS function, the exponent k of the function controls the affinity of an outflow for relatively younger or older water in storage. Specifically, $k < 1$ ($k > 1$) indicates that the outflow preferentially selects young (old) water available in the storage, where the lower (higher) the value of k, the higher the preference. In the case where $k = 1$, the released waters are sampled uniformly from the storage irrespective of their ages. We defined the power-law SAS functions of ET and R fluxes using a single, time-invariant parameter k (k_{ET} and k_{R}, respectively). Initial model tests revealed that the model results were not sensitive to variations of k_{R} over a wide range, possibly due to the small magnitude of R compared to other fluxes. Therefore, to reduce the number of model parameters, we fixed k_{R} at 1 (i.e., uniform selection) for following model runs.

Following Benettin et al. (2017), we considered two different model configurations to specify the SAS function of Q. The first model (Model 1) is a simpler model with a fixed power-law exponent k_Q. The second model (Model 2) attempts to assess the possible time variance of k_Q in response to storage variations. In this case, k_Q is made time-variant between two endmembers, $k_{Q\mathrm{dry}}$ and $k_{Q\mathrm{wet}}$, based on a normalized wetness index (wi; $wi \in [0,1]$) of the system. Therefore, $k_Q(t) = k_{Q\mathrm{wet}} + (1 - wi(t))/(k_{Q\mathrm{dry}} - k_{Q\mathrm{wet}})$ (Benettin et al., 2017), and $k_{Q\mathrm{dry}}$ and $k_{Q\mathrm{wet}}$ are the values of k_Q under the driest and wettest conditions, respectively. In practice, $wi(t)$ can be set proportional to the storage variations that are directly computed from a water mass balance using the daily hydrologic fluxes. However, uncertainties in the ET and R fluxes prevent accurate estimation of these variations, especially at short time scales. We therefore estimated wi using the dynamical system approach proposed by Kirchner (2009) by assuming that Q is itself the best gauge of the storage and, by extension, wi. Detailed description on the estimation of wi is provided in Text S1 in Supporting Information S1.

Table 1
Summary of the Calibration Parameters

Symbol	Definition	Range
$k_Q/k_{Q\mathrm{dry}}/k_{Q\mathrm{wet}}$	SAS parameter for Q	0.1–5[a]
k_{ET}	SAS parameter for ET	0.1–10[a]
K_{Cl}	Diffusion rate (d^{-1})	0.001–0.5[a]
S_0	Initial storage (mm)	200–2000

[a] Parameter values are drawn from log-transformed ranges.

3.5.3. Chloride Simulation

The specified SAS model was coupled to Equation 8 to simulate Cl concentrations in Q. Most previous studies that utilized Cl for water age estimation relied on the temporal fluctuations of Cl in precipitation and the subsequent dampening of these fluctuations in streamflow (e.g., Kirchner et al. (2010) and Harman (2015)). In these studies, Cl exchange between water parcels was restricted to preserve distinct input signals, although it is known that Cl in different water parcels can mix in the soil through diffusion (Porter et al., 1960). In our case, precipitation contained negligible Cl content, and soil water within the control volume was enriched in Cl due to legacy fertilizer input. Therefore, the strong concentration gradient in Cl between a newly arriving water parcel and older water parcels in its surroundings may promote Cl mixing through diffusive transport. Moreover, it has been shown that selective Cl uptake by ET can cause an enrichment of Cl concentration in storage (i.e., evapoconcentration), resulting in apparent Cl imbalances between input and output fluxes (Hrachowitz et al., 2015). In this study, inclusion of the evapoconcentration effect is supported by previous studies reporting low Cl content in corn and soybean grains (<0.04%) (Batal et al., 2011) and negligible crop Cl accumulation compared to river Cl export in the UER watershed (David et al., 2016). The evapoconcentration effect is also evident from the measured Cl concentration data, where concentration spikes were often observed near the peak GS with enhanced ET rates (Figure 2b). Therefore, to be consistent among the three study tiles and to reduce the number of parameters, we assumed that ET does not remove Cl from the storage.

The combined effect of Cl diffusive mixing and evapoconcentration were modeled using a Lagrangian approach that tracks the fate of individual water parcels as they transit through the system while aging (Queloz et al., 2015). To account for Cl diffusion, we adopted the method of Van der Velde, De Rooij, et al. (2010) and Van Der Velde et al. (2012), which employs an effective diffusion constant (K_{Cl}) to describe the rate of Cl redistribution from older to younger water parcels through diffusion. In practice, this process is modeled by using a first-order kinetic equation to simulate the tendency of all water parcels to approach a system-wide equilibrium Cl concentration (C_{eq}), determined by the overall Cl availability within the storage (Van der Velde, De Rooij, et al., 2010; van der Velde et al., 2012). A similar approach has been used to model the mass transfer of $\mathrm{NO_3}^-$ between a mobile and immobile phase in soil (Botter et al., 2005; Rinaldo & Marani, 1987). Therefore, assuming that a pulse of water enters the system at time t_i, the evolution of its Cl concentration driven by the Cl diffusion and evapoconcentration processes can be described as:

$$\frac{dC(T,T+t_i)}{dT} = K_{\mathrm{Cl}}\left(C_{\mathrm{eq}}(T+t_i) - C(T,T+t_i)\right) + \frac{ET(T+t_i)p_{\mathrm{ET}}(T,T+t_i)}{S(T+t_i)p_S(T,T+t_i)}C(T,T+t_i) \tag{12}$$

At each time step, C_{eq} is calculated from a Cl mass balance, which updates the total Cl mass in the storage by accounting for Cl loss through Q and R (Botter et al., 2005). While ET reduces the storage, it does not change the total Cl mass due to the evapoconcentration effect. Equation 12 was used to update $C_S(T, t)$ in Equation 8 at each time step to provide the required corrections for simulating $C_Q(t)$. Moreover, a sensitivity analysis was conducted to quantify how the parameterizations of Cl diffusion and evapoconcentration affect the modeled storage and water selection behaviors.

3.5.4. Model Calibration and Evaluation

The initial total water storage, S_0, is required for the age and Cl mass balance calculations and is kept as a calibration parameter. This results in four calibration parameters for Model 1 (k_Q, k_{ET}, K_{Cl}, S_0) and five for Model 2 ($k_{Q\mathrm{dry}}$, $k_{Q\mathrm{wet}}$, k_{ET}, K_{Cl}, S_0). Plausible uniform parameter ranges for all the parameters were estimated from the literature (Benettin et al., 2017; Van der Velde, De Rooij, et al., 2010) and field experience (Andino et al., 2020) and are given in Table 1. For each model, 10^6 simulations were run for each tile by randomly selecting parameter sets from the uniform prior ranges. The performance of the model was evaluated for the period of 2015–2020 water years using the Nash-Sutcliff Efficiency (NSE) and its logarithmic version ($\mathrm{NSE_{log}}$) of the simulated Cl concentrations. Given the characteristic trend in the Cl data, we used the whole time series from this period and did not divide the data into a calibration and validation period. Data collected during the 2021 and 2022 water years were not included in the calibration due to the complexity resulting from the potash application in 2021.

To minimize the impact of unknown initial conditions, the hydrologic fluxes from the calibration period were repeated twice to provide a spin-up period of 10 years. The water storage was initialized as a single age-ranked

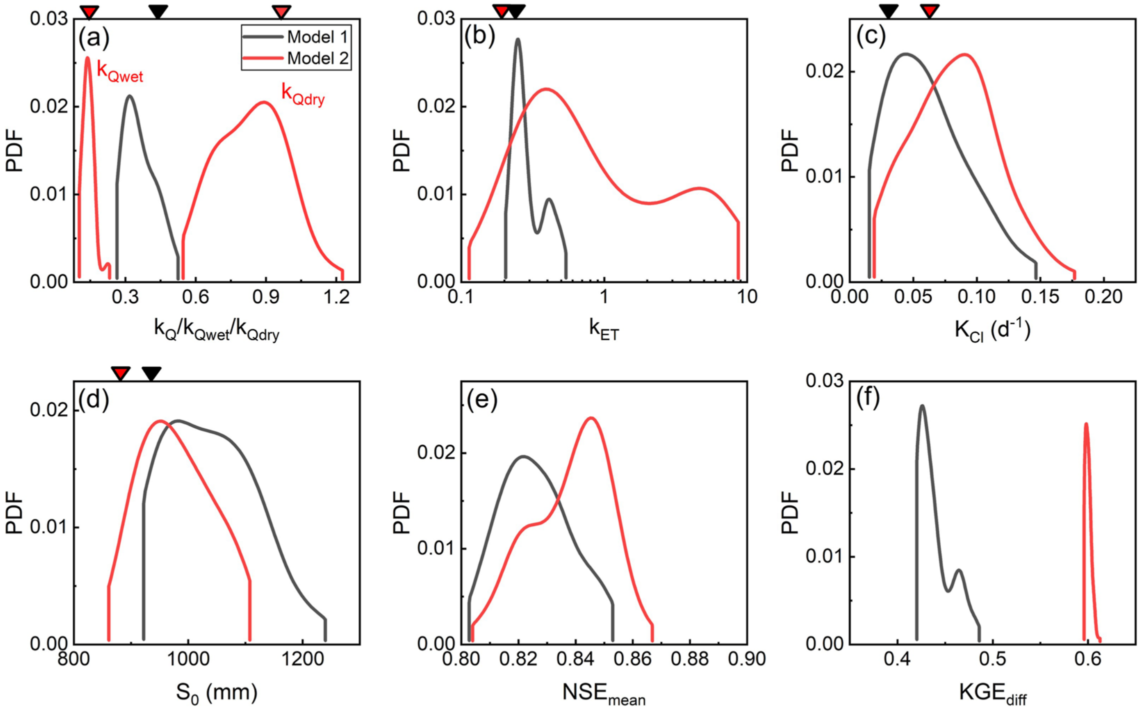

Figure 3. (a–d) Behavioral parameter distributions of Model 1 and Model 2 for Tile B. The distributions are smoothed using a normal kernel distribution. The optimal parameter values corresponding to the highest Kling-Gupta Efficiency (KGE) values for the detrended Cl concentration (KGE_{diff}) are indicated by triangles at the top axis. (e, f) Probability distributions of the mean value of Nash-Sutcliff Efficiency (NSE) and NSE_{log} (NSE_{mean}) and KGE_{diff} for the behavioral simulations.

storage with a prescribed high Cl concentration (i.e., 100 mg L^{-1}) at the beginning of the spin-up. After the spin-up period, the Cl concentrations were linearly scaled across the entire age-ranked storage so that the average Cl concentration in the storage equaled the 90th percentile of Cl concentrations measured in the 2015 water year. This value ranged from 11.5 to 14.3 mg L^{-1} for the three tiles. Additionally, the initial C_{eq} was calculated using the total Cl mass and the storage at the beginning of the calibration period. Daily time steps and an explicit Euler scheme were used to run the model for the spin-up period (Benettin & Bertuzzo, 2018b). The time step was reduced to 12 hr for the calibration period and the simulated Cl concentrations were extracted at the end of each day.

Results from initial model calibrations suggest that the use of NSE and NSE_{log} was not able to effectively identify behavioral parameter sets. This is because any parameter sets that could reproduce the general dilution trend in the Cl data would receive high NSE and NSE_{log} values, even though they performed poorly in simulating the transient Cl variability at short time scales. To address this issue, we adopted a sequential method by including a third performance measure based on the Kling-Gupta Efficiency (KGE) criterion (Kling et al., 2012). Specifically, we first calculated the first-time derivative of the Cl time series (ΔCl) to remove the long-term dilution trend. The model's capability in simulating the short-term Cl fluctuations was then assessed using the KGE of simulated ΔCl. Thus, in the first step of the model evaluation, the parameter sets giving NSE and NSE_{log} values higher than 0.8 were retained. In the second step, the retained parameter sets were ranked by decreasing KGE, and the top-ranked 100 sets were designated behavioral and used to compute water age distributions.

4. Results

4.1. Model Performance and Parameter Identification

Frequency distributions of the behavioral parameter sets are shown in Figure 3 for Tile B, and in Figures S3 and S4 in Supporting Information S1 for Tiles A and C, respectively. The corresponding behavioral parameter ranges are reported in Tables S1 and S2 in Supporting Information S1. The initial water storage S_0 and the SAS parameters of Q were clearly identified under both model configurations. In general, S_0 ranges between 800 and

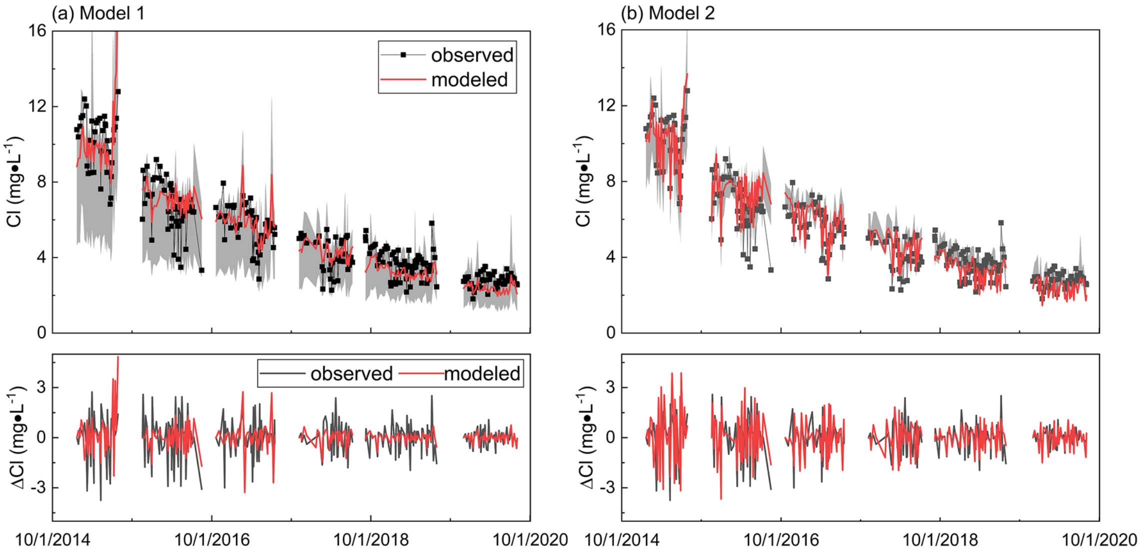

Figure 4. Simulations of the Cl concentrations and the detrended Cl concentrations (ΔCl) based on (a) Model 1 and (b) Model 2 compared to measured data (black dots) for Tile B. Red lines indicate simulations based on the optimal parameter sets. Gray bands indicate the envelope of the behavioral simulations.

1,200 mm for the three tiles, regardless of the model configuration (Figure 3d, Figures S3d and S4d in Supporting Information S1). For Model 2, a prominent inverse storage effect was revealed by the behavioral distributions of $k_{Q\mathrm{wet}}$ and $k_{Q\mathrm{dry}}$, where $k_{Q\mathrm{wet}}$ is significantly lower than the paired $k_{Q\mathrm{dry}}$, and the values of $k_{Q\mathrm{dry}}$ are relatively close to a uniform selection scheme (Figure 3a, Figures S3a and S4a in Supporting Information S1). On the other hand, when k_Q is not allowed to vary, the behavioral distributions of k_Q consistently fall in between the values of $k_{Q\mathrm{wet}}$ and $k_{Q\mathrm{dry}}$ and reflect a clear preference for the younger stored water (Figure 3a, Figures S3a and S4a in Supporting Information S1). The behavioral K_{Cl} generally ranges between 0.01 and 0.2 days^{-1} based on both models (Figure 3c, Figures S3c, S4c, and Table S2 in Supporting Information S1), suggesting that it takes 5–100 days for a water parcel to reach the equilibrium concentration dictated by the Cl mass balance. Finally, the parameter k_{ET} of Model 1 was relatively well constrained and indicates that ET has a high affinity for the younger stored water (Figure 3b, Figures S3b and S4b in Supporting Information S1). In contrast, the values of k_{ET} based on Model 2 span a large fraction of the prior range, suggesting large parameter uncertainty, although values lower than 1 were more likely to yield a better model performance (Figure 3b, Figures S3b and S4b in Supporting Information S1). A closer look into the relationships between the model parameters revealed a significant negative correlation between k_Q and k_{ET} in Model 1 (Table S3 in Supporting Information S1) and between $k_{Q\mathrm{wet}}$ and k_{ET} in Model 2 (Table S4 in Supporting Information S1). Additionally, there is a significant positive correlation between k_{ET} and K_{Cl} in both models (Tables S3 and S4 in Supporting Information S1). Therefore, it is the combination of these parameters that determines the simulated Cl transport dynamics, rather than the values of the individual parameters.

The simulated Cl concentrations and ΔCl are compared to the measured data in Figure 4, Figures S5 and S6 in Supporting Information S1 for the three tiles. Although both models are excellent in reproducing the salient dilution trend in the Cl data, the marked short-term Cl responses are better captured by the behavioral simulations of Model 2. This is supported by an increase in the KGE value from 0.33–0.47 to 0.43–0.60 across the three tiles (Figure 3f, Figures S3f and S4f in Supporting Information S1). Interestingly, although k_{ET} was poorly identified for Model 2, the envelope of simulated Cl concentrations based on the behavioral parameter distributions of Model 2 is narrower than that derived based on Model 1, indicating a tradeoff between model error and parameter identifiability (Rodriguez & Klaus, 2019).

4.2. Tile Discharge Age Distributions

The median age of Q is shown in Figure 5 for Tile B, along with the time series of J, ET, Q, and wi. We used median age (i.e., the age which is not exceeded by 50% of the water particles), instead of mean age, because it is less sensitive to uncertainties in the older water fractions. There are marked differences between the median age

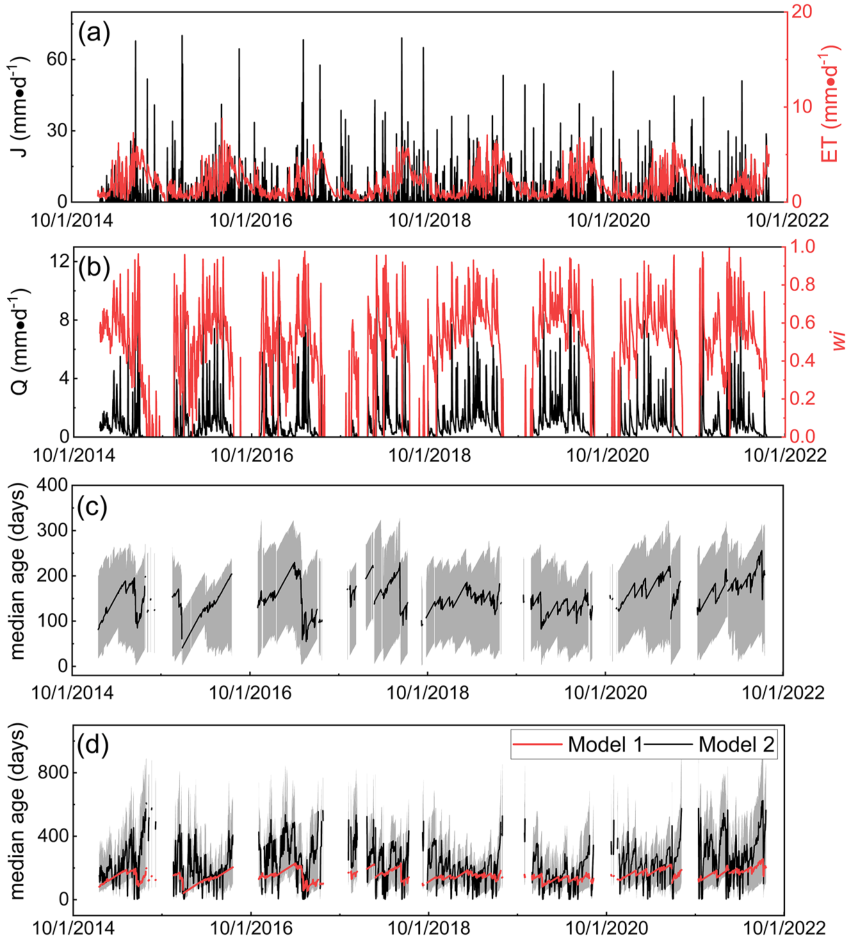

Figure 5. Daily variations in key hydrologic fluxes and median tile discharge age of Tile B. (a) Precipitation and evapotranspiration fluxes. (b) Tile discharge and the normalized wetness index (*wi*) of Tile B. (c) Median age of tile discharge derived based on Model 1. Black line indicates simulation based on the optimal parameter set. Gray bands indicate the envelope of the behavioral simulations. (d) Same as (c), but based on Model 2. The optimal simulation based on Model 1 is also shown in panel (d) to aid comparison between the two models.

estimated by using the two models. For the fixed k_Q, the median age varies relatively little around a mean value, although this mean value varies from about 50 to 230 days among the behavioral paraments sets (Figure 5c). In contrast, for the storage-dependent case (i.e., Model 2), the median age spans a wide range of 3 days to more than 800 days and is highly responsive to variations in Q (Figure 5c). More specifically, the median age decreases approximately exponentially with increasing rates of Q, indicating increasing young-water dominance during high flow events (Figure S7 in Supporting Information S1). This inverse relationship between the median age and Q is a direct product of the inverse storage effect and is expected since Q was used to derive *wi* (see Text S1 in Supporting Information S1). Where k_Q is stationary (i.e., $k_{Q\mathrm{wet}} = k_{Q\mathrm{dry}}$), however, the median age does not have an appreciable relationship with Q (Figure S7 in Supporting Information S1).

The daily age distributions of Q were weighted by Q and averaged to obtain the marginal age distribution for the three tiles. The marginal distribution represents the long-term average behavior of the system and is therefore a useful metric to characterize system properties (Benettin et al., 2017). The marginal distributions generated from the optimal behavioral parameter sets (i.e., the sets leading to the highest KGE values; Figure 3, Tables S1 and S2 in Supporting Information S1) are shown in Figure 6. For each tile, adopting the storage-dependent k_Q results in a larger proportion of young water compared to the fixed k_Q scenario. Based on Model 2, the marginal distributions predict that, on average, 29%–34% of Q was younger than 10 days for the three tiles, while 45%–50% was older than 100 days. Model 2 also predicts that 69%–76% of Q measured at the three tiles was younger than 1 year and 13%–20% older than 2 years. Finally, based on Model 2, the median age of Q was, on average, 81, 104, 66 days for Tiles A, B, and C, respectively. These results are generally consistent with the 45 days reported by Danesh-Yazdi et al. (2016) for soil

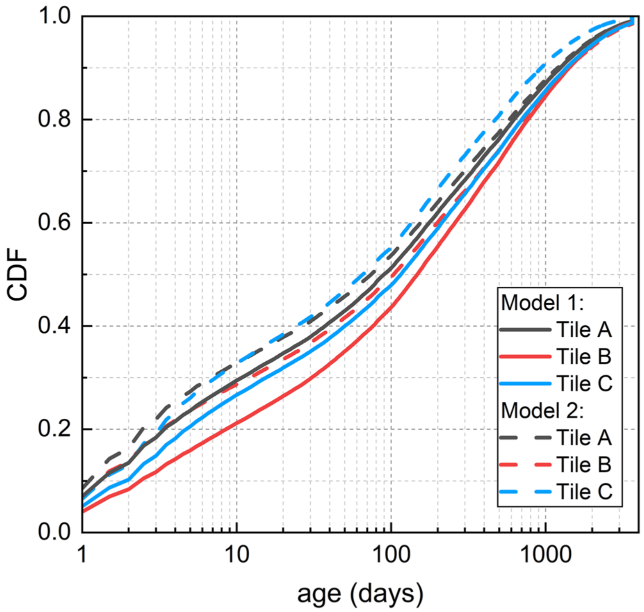

Figure 6. Marginal age distribution of tile discharge based on the optimal parameter sets of Model 1 and Model 2 for the three study tiles. Note that water ages higher than 3,650 days (i.e., 10 years) are grouped into the 3650-day category.

root zone discharge of a tile-drained watershed in southern Minnesota using a conceptual SAS modeling approach.

4.3. Nitrate Export Regime and the Relationship Between NO_3^- Export and Water Age

The estimated *b* value of the log-log regression of NO_3^- concentration and tile discharge is essentially zero (i.e., $|b| < 0.05$) for all three crop seasons (Figure 7a). Moreover, the relationship between tile discharge and daily NO_3^- load is significantly linear ($p < 0.01$, ordinary linear regression; Figure 7b), suggesting that the variance of NO_3^- export was dominated by the variance of discharge. These results indicate a persistent chemostasis in NO_3^- export over time. However, the slope of the discharge-load relationship is higher for the corn GS compared to the soybean year and the NGS of corn (Figure 7b), highlighting the impact of fertilizer input on tile NO_3^- loads. Additionally, although lower than the threshold value for nonlinear chemodynamic export (i.e., 0.5), the calculated CV_C/CV_Q value is higher in the corn GS (0.37) compared to the other two seasons (0.27 and 0.28; Figure 7a).

To investigate the relationship between NO_3^- export and water age, we defined a median age anomaly as the difference between the median age of tile discharge and the discharge-weighted mean median age using the optimal parameter set of Model 2 for each tile. Because this metric accounts for the difference in the mean median age among the three tiles, it can be directly combined and compared to NO_3^- concentrations and daily NO_3^- loads for the three tiles. While no clear correlation is found between the median age anomaly and NO_3^- concentration measured during the soybean year and the corn NGS (Figure 7c), NO_3^- concentrations measured during the corn GS are negatively correlated with the median age anomalies ($p < 0.01$, ordinary linear regression; Figure 7c), suggesting that higher NO_3^- concentrations in tile discharge were associated with the release of younger stored water during this period. The relationship between the median age anomaly and NO_3^- load is consistent among the three tiles and exhibits a similar exponential pattern, where the NO_3^- load decreases exponentially with increasing median age anomaly. This exponential relationship is a direct product of the linear relationship between daily NO_3^- load and tile discharge (i.e., chemostasis; Figure 7b) and the inverse relationship between the median age and discharge (i.e., the inverse storage effect; Figures S7d–S7f in Supporting Information S1).

4.4. Nitrate Isotope Dynamics

Nitrate isotope measurements revealed unique temporal patterns in the $\delta^{15}N$ and $\delta^{18}O$ values of tile drainage NO_3^- (Figure 8, Figures S8 and S9 in Supporting Information S1). During the NGS of corn, the $\delta^{15}N$ and $\delta^{18}O$ values ranged from 5–10‰ to 4–8‰, respectively, both showing a steady decline of 4–5‰. Following the pre-plant and side-dress N applications, low $\delta^{15}N$ and $\delta^{18}O$ values (e.g., −5‰ and −1‰, respectively) were observed concurrently with a dramatic increase in NO_3^- concentrations (Figure 8, Figures S8 and S9 in Supporting Information S1). Measured $\delta^{15}N$ values of potential N sources for tile drainage NO_3^- (i.e., fertilizer and soil organic N) were consistently close to or higher than 0‰ (not shown), suggesting that the low $\delta^{15}N$ values of NO_3^- resulted from the nitrification of surface-applied ammoniacal fertilizers (detailed discussion on the fertilizer and soil isotope data will be presented in a future publication). However, this period of low $\delta^{15}N$ and $\delta^{18}O$ values was relatively short-lived, as they rapidly increased with decreasing tile discharge toward the end of the GS (Figure 8, Figures S8 and S9 in Supporting Information S1). The $\delta^{15}N$ and $\delta^{18}O$ values measured during the soybean year are similar to those measured near the end of the corn season (Figure 8, Figures S8 and S9 in Supporting Information S1). Compared to NO_3^- concentrations, the measured $\delta^{15}N$ and $\delta^{18}O$ values were much more responsive to changes in tile discharge, especially during the soybean year and the NGS of corn, with marked declines coinciding with high flow events (Figure 8, Figures S8 and S9 in Supporting Information S1).

Comparing the $\delta^{15}N$ and $\delta^{18}O$ values of NO_3^- revealed prominent denitrification trends in the dual isotope space (Figures 9a, 9c, and 9e). The slopes of the denitrification lines are close to or lower than 1, ranging from 0.5 to

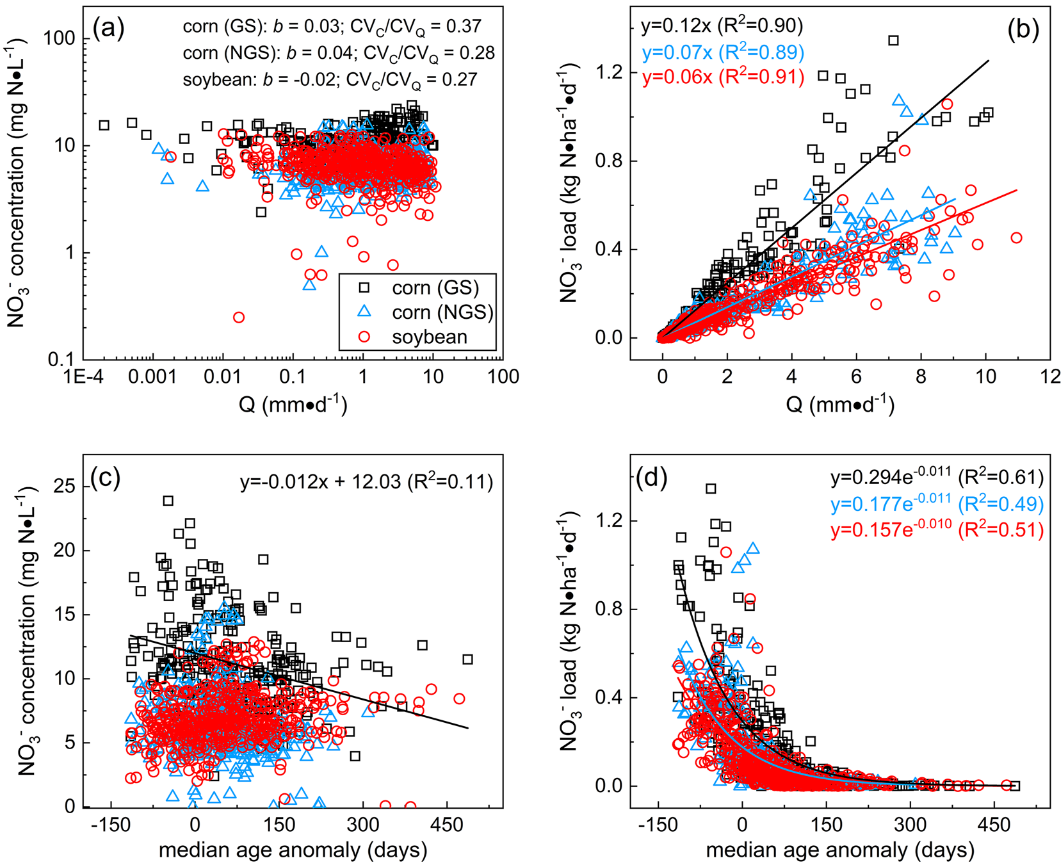

Figure 7. Relationships between (a) tile discharge and NO_3^- concentration, (b) tile discharge and daily NO_3^- load, (c) median age anomaly and NO_3^- concentration, and (d) median age anomaly and daily NO_3^- load. These relationships are examined for three crop seasons: corn growing season, corn nongrowing season, and soybean year. The estimated b and CV_C/CV_Q values for categorizing NO_3^- export regime are shown in panel (a). Regression lines and equations for statistically significant relationships are also provided in panels (b–d).

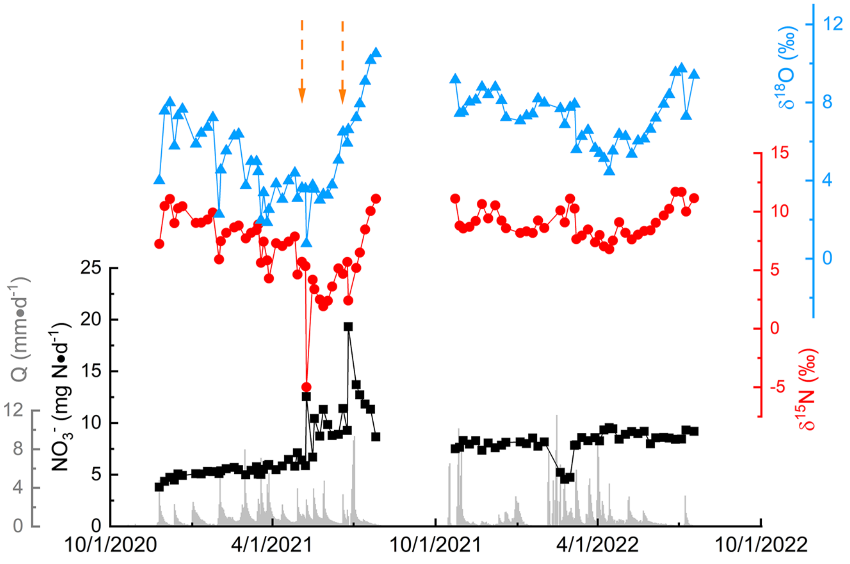

Figure 8. Temporal dynamics of NO_3^- concentrations and isotopes measured at Tile B during the 2021 and 2022 water years. Daily tile discharge rates are shown in the bottom to aid interpretation. Dashed orange arrows denote the timing of spring pre-plant and side-dress N fertilizer applications.

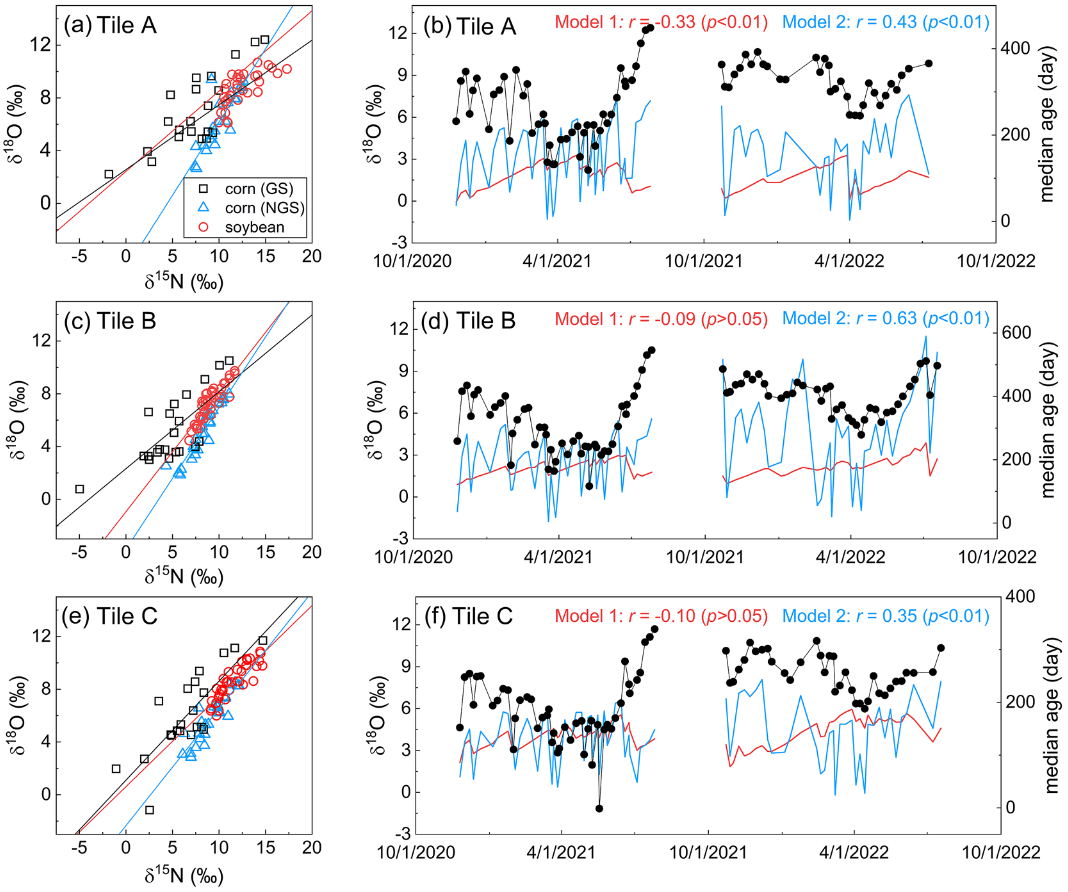

Figure 9. (a, c, and e) Relationships between δ^{15}N and δ^{18}O values of NO_3^- during the corn growing season, corn nongrowing season, and soybean year. Solid lines represent statistically significant regression lines between δ^{15}N and δ^{18}O values of NO_3^-. (b, d, and f) Comparisons between the δ^{18}O of NO_3^- and the median age estimated based on Model 1 and Model 2. The Pearson's correlation coefficient for each comparison is also shown.

1.1 across different tiles and different crop and growing phases. To further investigate how this denitrification imprint varies with water age, we compared δ^{18}O values of NO_3^- with the median age of tile discharge that was simulated using the optimal parameter set of each tile for the 2021 and 2022 water years (Figures 9b, 9d, and 9f). In this case, a higher δ^{18}O value indicates a larger extent to which the NO_3^- in tile discharge has undergone denitrification. The δ^{18}O of NO_3^- is significantly and positively correlated with the median age estimated based on Model 2 for all three tiles ($p < 0.01$, Pearson's r; Figures 9b, 9d, and 9f). Importantly, the temporal variability of δ^{18}O closely resembles the flashy responses inherent in the median age of tile discharge, especially during the corn year. Conversely, the δ^{18}O of NO_3^- and the median age estimated based on Model 1 either lack correlation (Figures 9d and 9f) or exhibit a negative correlation due to counteracting variations at the seasonal scale (Figure 9b). Due to the strong correlations between the two isotopes (Figures 9a, 9c, and 9e), substituting δ^{18}O values of NO_3^- with δ^{15}N values does not alter the results of this correlation analysis with water age.

5. Discussion

5.1. How Does the Age of Tile Discharge Vary With Hydroclimatic Conditions and Reflect Activation of Distinct Flow Paths?

Although the mean median age does not differ significantly between Model 1 and Model 2 (Figure 6), implementing the storage-dependent k_Q leads to a unique water age dynamic that is characteristic of an inverse storage effect (Harman, 2015). A definitive identification of the inverse storage effect is challenging in our case due to the salient trend in the Cl data as well as the uncertainties in the boundary conditions and input fluxes (e.g., R) which may have compromised the model calibration and evaluation process. For example, although Model 2 consistently has higher KGE values than Model 1, the increase is only modest (i.e., by 0.1–0.15 unit) given that Model 2 is more complex, and the parameter k_{ET} is more uncertain when k_Q is allowed to vary. This, along with the significant correlations between the model parameters (Tables S3 and S4 in Supporting Information S1), underscores the difficulty in overcoming the equifinality for both parameter identification and model selection (Beven, 2006), even for parsimonious models with only 4–5 parameters. However, while the measured NO_3^- concentrations were largely insensitive to variations in the modeled water age (Figure 7c), the temporal dynamics of NO_3^- isotopes can only be mechanistically explained by the inverse storage effect (Figures 9b, 9d, and 9f). Specifically, the positive correlation between NO_3^- isotopes and water age depicts a coupled water and NO_3^- transport, where young water integrates short flow paths that transmit NO_3^- from nitrification-dominated surface soil layers. In contrast, aged water typically originates from deeper subsurface layers in which anoxic conditions and longer contact times between NO_3^-, organic carbon, and microbes enhance NO_3^- denitrification. This distinct and consistent correlation between NO_3^- isotopes and water age estimated based on Model 2 provides strong evidence that the revealed inverse storage effect is not a result of model overparameterization and overfitting but reflects intrinsic water mixing and selection mechanisms at the tile-drain scale. The unique strength of NO_3^- isotopes in this case results from their inherent sensitivity to biogeochemical NO_3^- transformation processes, the net effects of which are often too subtle to discern by NO_3^- concentration measurements. Therefore, the main relevance of this work is the use of NO_3^- isotopes, a biogeochemical tracer, to corroborate water mixing and selection behaviors simulated by SAS functions. It complements the emerging tenet that advancing the knowledge of water age dynamics leads to a better understanding of reactive solute transport (Hrachowitz et al., 2016) by demonstrating that the latter can also benefit the former. More discussion on the utility of NO_3^- isotopes in modeling reactive NO_3^- transport is presented in Section 5.3.

The positive diagnosis of an inverse storage effect provides useful insights into how flow paths contributing to tile discharge are rearranged and repartitioned under different hydroclimatic conditions. In fine-textured soils with high root density conditions, the inverse storage effect may be explained by an extensive network of vertically oriented preferential flow paths (i.e., macropores associated with root channels, earthworm burrows, desiccation cracks), combined with a threshold-driven interaction between the preferential flow paths and the soil matrix. Specifically, when antecedent soil moisture is low, precipitation water infiltrates the soil matrix, and only a small amount of event water and mobilized soil matrix water reaches the tile drain via preferential flows (Cain et al., 2022; Williams et al., 2016). Once a moisture threshold is reached and further exceeded within upper soil layers, progressively more preferential flows are initiated at near saturated surface soil layers, which subsequently bypass the lower soil matrix due to a reduced matrix-macropore interaction under high soil moisture conditions (Hrachowitz et al., 2013; Klaus et al., 2013). The preferential recharge at the upper part of the saturated zone may, therefore, activate lateral short flow paths toward the tile drain (Jiang & Somers, 2009), leading to an increased probability of relatively young water being selected for tile discharge. Conversely, during recession periods, the groundwater table continuously subsides, and the network of preferential flow paths shrinks. As a result, a large portion of younger stored water is retained in the unsaturated zone, where the flow regime is dominated by percolation again. The downward displacement of soil matrix water increases the relative contribution of deep and long flow paths that remain connected with the tile drain. This results in declining probability that water with relatively young age is selected for discharge. Therefore, the age dynamics of tile discharge are modulated by a storage-dependent interplay between slow percolation and fast recharge through preferential flows. This mechanism explains the dynamical system analysis that revealed a threshold-like storage dependence of tile discharge at our study tiles (Figure S2 and see Text S1 in Supporting Information S1). It is also consistent with conclusions drawn from other tile drainage studies conducted in the Midwestern U.S., where large contributions of event water in tile discharge (e.g., up to 80%) underscore the prevalence of preferential flow paths in densely cropped tile-drained systems (Stone & Wilson, 2006; Vidon & Cuadra, 2010; Williams et al., 2016).

The total storage was estimated to be about 1,000 mm for the three tiles (Figure 3d). Assuming an average porosity of 0.4 for silty loam Mollisol (Franzmeier, 1991), this storage would require a soil depth of at least 2.5 m, which corresponds to the entire above-tile soils plus an additional 1 m of soils below the tile drain. This implies that water stored below the tile drain is involved in water and solute mixing during discharge generation. One way to reconcile this apparently large mixing volume with the high affinity of tile discharge for young water is to examine the age-ranked storage that contributes to tile discharge. Based on the optimal parameter sets of Model 2, the median and 80th percentile of the age-ranked storage that was tapped to generate tile discharge were 120–154 mm and 444–518 mm, respectively, for the three tiles. If we assume that the residence time, and thus ranked age of water, generally increases with soil depth (Asano & Uchida, 2012), these age-ranked storage volumes indicate that 50% and 80% of tile discharge originated from the first 0.4 and 1.2 m of the soil profile. Thus, the age of tile discharge is better explained by the amount of hydrologically connected storage than by the total storage. On the other hand, however, there is substantial storage below the tile drain (i.e., on the order of 400–600 mm) that provides a small contribution to tile discharge, yet produces the oldest water that constitutes the upper end of the marginal age distribution (e.g., >2 years) (Figure 6). This below-tile storage, therefore, represents a legacy store that retains long memory of past water and solute inputs due to a slow turnover rate (Woo & Kumar, 2019). Taken together, even though flow paths are vertically oriented at the tile-drain scale, the tile drain system can be viewed as a microcosm of a sloping watershed, where main flow paths vary between shallow and deep subsurface as different storage compartments become hydrologically connected to or disconnected from streams.

It is important to note that the estimated total storage and water age distributions are conditioned on the estimated R fluxes and the implemented modeling schemes for Cl diffusion and evapoconcentration. An informal sensitivity analysis showed that varying the R fluxes over the range of 50%–150% of their original values (with corresponding changes in the ET fluxes to close the water balance) had a negligible influence on the estimated storage and water age statistics. Further justification of the R fluxes (e.g., for its temporal variations) is difficult due to the lack of direct measurements. On the other hand, excluding Cl diffusion or allowing ET to remove Cl from storage had a significant impact on the estimated total storage. Taking Tile B as an example, if we do not consider Cl diffusion in the SAS modeling (i.e., $K_{\mathrm{Cl}} = 0$ days^{-1}), S_0 becomes poorly identified (behavioral range: 356–1986 mm), and the optimal value (540 mm) is lower than that estimated based on Model 2 (883 mm) (Figure S10 in Supporting Information S1). Furthermore, if we split the total ET into evaporation and transpiration fluxes and allow transpiration to remove Cl from storage, the range of behavioral S_0 shifts upward to 1,657–2,497 mm (Figure S11 in Supporting Information S1). This revealed high sensitivity in estimating the total storage stems from the limited information content of Cl for tracing old water, as well as the lack of direct tracer measurements for ET, which are indeed a structural problem in SAS-based transport modeling (Benettin et al., 2022) (more details about the sensitivity analysis results are provided in Text S2 in Supporting Information S1). However, regardless of the parameterizations of Cl diffusion and evapoconcentration, the fundamental age selection behavior of tile discharge (i.e., the young water preference and inverse storage effect) is robust across different modeling scenarios (Figures S10 and S11 in Supporting Information S1). Moreover, the mean median age of tile discharge can be constrained into a narrow range (74–104 days for Tile B; Figure S12 in Supporting Information S1), despite the uncertainties in estimating the total storage and the water selection behavior of ET (see Text S2 in Supporting Information S1). These results, together with the consistency of age selection behaviors revealed among the three tiles, provide a degree of confidence in our estimated water age.

5.2. How Does Tile NO_3^- Export Respond to Variations in Tile Water Age?

Combining water age modeling with NO_3^- isotope measurements provides an opportunity to unravel dominant hydrological and biogeochemical mechanisms that control NO_3^- export at the tile-drain scale. Despite the large and often vigorous variations in tile water age, NO_3^- concentrations remained largely stable during both the soybean year and the NGS of corn (Figures 2a and 7a). On the other hand, the measured NO_3^- isotopes were positively correlated with water age (Figure 9), implying a relative dominance of nitrification over denitrification and thus a surface origin of NO_3^- when tile discharge is high. These somewhat paradoxical findings can be partially reconciled by a large mixing volume as generally suggested by the SAS modeling, which dampens concentration variations relative to tile discharge (Basu et al., 2010). Moreover, the observed NO_3^- export regime and isotope dynamics may also indicate a relatively homogeneous distribution of NO_3^- across the soil profile. Specifically, while NO_3^- concentrations might be higher in younger stored water due to relatively fast mineralization and nitrification rates in shallow soil layers, the contrast in NO_3^- concentration between shallow and deep soil horizons was not substantial enough to induce significant deviations from chemostasis. Indeed, using numerical simulations, Musolff et al. (2017) demonstrated that chemostasis can result from the absence of strong solute attenuation along a defined flow path. The inferred relative homogeneity in NO_3^- distribution thus implies that denitrification was not sufficiently rapid to deplete NO_3^- in the older stored water. As a result, NO_3^- concentrations in tile discharge remained largely stable, despite the variable mixing of younger and older water during tile discharge generation.

Based on the above discussion for the soybean year and NGS of corn, one might expect that tile NO_3^- export would exhibit a flushing pattern following N fertilizer applications due to a substantial increase in NO_3^- concentration in near-surface soil horizons. Indeed, the very low NO_3^- isotope values observed during this critical period indicate the rapid movement of fertilizer-derived NO_3^- to the tile drains (Figure 8, Figures S8 and S9 in Supporting Information S1). Moreover, the significant, albeit weak, inverse correlation between NO_3^- concentrations and the median age anomalies of tile discharge is also in line with a flushing export regime in conceptual terms (Figure 7c). However, NO_3^- export regime remained chemostatic during the GS of corn (Figures 7a and 7b). The absence of flushing export during this period may be explained by two reasons. First, NO_3^- derived from fertilizer nitrification might quickly migrate to greater soil depths via preferential flows, which consequently dampened the vertical contrast in NO_3^- concentration. Previous studies have shown that solute exchange fluxes between penetrated soil macropore water and the surrounding matrix water are dominantly unidirectional, from macropores to the soil matrix (Woo & Kumar, 2019). The rapid downward migration of fertilizer-derived NO_3^- via preferential flows could therefore lead to localized NO_3^- "hotspots" along the soil profile, giving rise to a more scattered concentration-discharge relationship and thus the higher CV_C/CV_Q value observed during this period (Figure 7a). The second explanation for the lack of NO_3^- flushing is the relatively low frequency of our sample collection (i.e., weekly), which might have missed "hot moments" of NO_3^- export following N fertilizer applications. Recent studies utilizing high-frequency measurements at the tile-drain scale have demonstrated substantial hysteretic and non-chemostatic patterns in event-based NO_3^- export (Liu et al., 2020). Future studies that adopt high sampling frequencies for both concentration and isotope measurements are warranted to better characterize the NO_3^- export regime and its relationship with water age. In sum, by coupling water age modeling with NO_3^- isotopic analysis, we are able to differentiate between the relevant biogeochemical and hydrological processes that control NO_3^- transport, which helps to delineate NO_3^- export dynamics at the tile-drain scale.

5.3. What Added Value Can NO_3^- Isotope Measurements Provide in Terms of Modeling Coupled Water and NO_3^- Transport?

We have shown that NO_3^- isotopes contain unique biogeochemical imprints, which in our case are useful to test competing hypotheses regarding water mixing and selection behaviors. To further explore the utility of NO_3^- isotopes for modeling NO_3^- transport under transient conditions, we modified a simple water age-based NO_3^- transport model previously proposed by van der Velde et al. (2012) by embedding isotope simulation into the model. In this simple model, NO_3^- concentration (C_{NO3}) in discharge is simulated by a convolution of time-variant water age distributions (i.e., $p_Q(T,t)$) with a constant relation between water age and NO_3^- concentration that is collectively determined by NO_3^- diffusive mixing and denitrification:

$$C_{\mathrm{NO3}}(t) = \int_0^{\infty} C_{\mathrm{eq}}\left(1 - e^{-k_d T}\right) e^{-k_n T} p_Q(T,t)\,dT \tag{13}$$

In Equation 13, k_d is the effective diffusion constant of NO_3^-, k_n is the first order rate constant of denitrification, and C_{eq} is the effective equilibrium NO_3^- concentration resulting from all NO_3^- source and sink processes in the soil, analogous to the C_{eq} used for modeling diffusive Cl mixing in the SAS model. Therefore, in this model, an infiltrating water parcel progressively approaches the effective equilibrium concentration due to mixing with surrounding waters, whereas, at the same time, the longer time it travels within the system, the more denitrification it experiences that reduces its NO_3^- concentration (van der Velde et al., 2012).

Here, we adopted this modeling scheme to simulate not only C_{NO3} but also the concentrations of the O isotope species of NO_3^- (i.e., the NO_3^- isotopologues) (Equations 14 and 15).

$${}^{16}C_{\mathrm{NO3}}(t) = \int_0^{\infty} {}^{16}C_{\mathrm{eq}}\left(1 - e^{-k_d T}\right) e^{-{}^{16}k_n T} p_Q(T,t)\,dT \tag{14}$$

$${}^{18}C_{\mathrm{NO3}}(t) = \int_0^{\infty} {}^{18}C_{\mathrm{eq}}\left(1 - e^{-k_d T}\right) e^{-{}^{18}k_n T} p_Q(T,t)\,dT \tag{15}$$

$${}^{18}\alpha_n = {}^{16}k_n/{}^{18}k_n \rightarrow {}^{18}k_n = {}^{16}k_n/\left({}^{18}\varepsilon_n/1000 + 1\right) = k_n/\left({}^{18}\varepsilon_n/1000 + 1\right) \tag{16}$$

In Equations 14 and 15, ${}^{16}C_{\mathrm{NO3}}$ and ${}^{18}C_{\mathrm{NO3}}$ are the concentrations of the major NO_3^- isotopologue $N^{16}O^{16}O^{16}O$ and the singly ${}^{18}O$-substituted isotopologue $N^{18}O^{16}O^{16}O$, respectively. Correspondingly, ${}^{16}C_{\mathrm{eq}}$ and ${}^{18}C_{\mathrm{eq}}$ denote the equilibrium concentrations of $N^{16}O^{16}O^{16}O$ and $N^{18}O^{16}O^{16}O$ in the soil. The first-order rate constant of

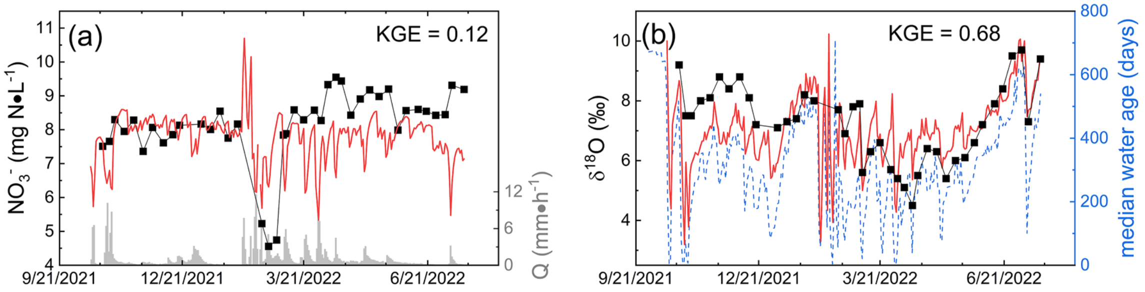

Figure 10. Results from the isotopologue-specific NO_3^- transport model. (a) Measured and modeled NO_3^- concentrations during the 2022 water year. Daily tile discharge rates were shown in the bottom to aid interpretation. (b) Measured and modeled $\delta^{18}O$ of NO_3^- during the 2022 water year. The median water age derived using the optimal parameter set of Model 2 was also shown to aid interpretation.

denitrification for $N^{18}O^{16}O^{16}O$ ($^{18}k_n$) was modeled by linking the rate constant for $N^{16}O^{16}O^{16}O$ ($^{16}k_n$) with the kinetic O isotope fractionation factor, $^{18}\alpha_n$, or equivalently the isotope effect, $^{18}\varepsilon_n$ (Equation 16). Note that by convention, $^{16}k_n = k_n$. As such, denitrification not only reduces the bulk concentration of NO_3^- but also simultaneously increases $^{18}C_{NO3}$ relative to $^{16}C_{NO3}$ (and thus $\delta^{18}O$) due to the kinetic isotope effect that results in a lower $^{18}k_n$ than $^{16}k_n$. This link between concentration, reaction kinetics, and kinetic isotope effect provides an important new dimension to constrain the coupled variations in NO_3^- concentration and isotopes driven by denitrification. Although $\delta^{15}N$ values of NO_3^- also contain valuable information, our focus here is on the $\delta^{18}O$ of NO_3^-. This approach helps us avoid complications related to potential changes in NO_3^- sources (such as fertilizer vs. soil organic N) and the subsequent variations in the $\delta^{15}N$ of the N substrates used for NO_3^- production. We omitted the kinetic isotope effect for NO_3^- diffusion because it is negligible compared to $^{18}\varepsilon_n$ (e.g., <1‰) (Mnich & Houlton, 2016).

To simulate the coupled NO_3^- concentration and isotope dynamics using Equations 13–15, we first calculated $^{16}C_{NO3}$ and $^{18}C_{NO3}$ using the measured NO_3^- concentrations and $\delta^{18}O$ values at each sampling point (see Appendix A for details of this isotopologue calculation). Moreover, we used water age distributions derived from the optimal parameter sets of Model 2 for $p_Q(T, t)$ in Equations 13–15 and set k_d to be equal to the optimal Cl diffusion constant (i.e., K_{Cl}). Therefore, given two independent constraints (i.e., C_{NO3} and $\delta^{18}O$), if we know the $\delta^{18}O$ of NO_3^- under equilibrium and the kinetic isotope effect for denitrification ($^{18}\varepsilon_n$), the system of Equations 13–15 can be inverted to solve for the two unknown parameters C_{eq} and k_n. For this proof-of-concept case, we assumed that C_{eq} is constant and that the $\delta^{18}O$ of NO_3^- under equilibrium is 0‰, which can be subsequently used to calculate $^{16}C_{eq}$ and $^{18}C_{eq}$ for any given C_{eq} (see Appendix A). This assumption essentially states that if there is no denitrification, the $\delta^{18}O$ of NO_3^- in tile discharge should reflect the isotopic signature of nitrification. The $\delta^{18}O$ value we assigned for nitrification-produced NO_3^- (i.e., 0‰) falls within the range of the lowest $\delta^{18}O$ values observed across the three tiles (i.e., −1.2 to 2.2‰) (Figure 9) and is consistent with results from previous studies based on nitrifier pure cultures (Buchwald & Casciotti, 2010). Furthermore, $^{18}\varepsilon_n$ was assumed to be 15‰, a value within the range obtained from laboratory soil incubations (e.g., 5–25‰ (Denk et al., 2017)) and commonly used to interpret NO_3^- isotopes measured at the watershed scale (Fang et al., 2015). Since C_{eq} was assumed to be constant during the simulation period, we applied the isotopologue-specific NO_3^- transport model only to the 2022 soybean year, during which C_{eq} was presumably much less variable compared to corn years. The unknown parameters C_{eq} and k_n were then determined using a nonlinear optimization algorithm based on the Levenberg-Marquardt method.

Since similar results were obtained for all three tiles, we will focus our discussion on the model simulation for Tile B. The simple NO_3^- transport model did not simulate NO_3^- concentrations well, particularly during the GS of soybean (i.e., starting from late April 2022), where the model largely underestimated NO_3^- concentrations in tile discharge (Figure 10a). This poor simulation may be simply explained by a time-variant C_{eq} even during soybean years due to continuous soil N cycling and soybean N uptake, which was not modeled in our case. However, despite the poor simulation of NO_3^- concentrations, the $\delta^{18}O$ of NO_3^- was well reproduced by the simple transport model (Figure 10b). This is supported by a KGE value of 0.68 for the simulated $\delta^{18}O$ values. Particularly encouraging is that the simple transport model was able to reproduce the dominant mode of variations in the $\delta^{18}O$ values between high- and low-flow conditions, which arise from distinct tile water ages due to the inverse storage effect (Figure 10b). Based on this simulation, C_{eq} and k_n were estimated to be 22.4 mg N L^{-1} and

0.0018 days^{-1}, respectively. The estimated k_n corresponds to a denitrification timescale of about 550 days. Given that the flow-weighted median water age for the simulation period was 134 days, this inferred denitrification timescale suggests that NO_3^- export from the tile-drain system was dominated by transport (Kumar et al., 2020). It is important to note that the results from this modeling exercise are qualitative, as they are contingent to the assumed isotopic signatures for nitrification (0‰) and the isotope effect for denitrification (15‰). However, the fact that the observed $\delta^{18}O$ values can be well reproduced by the commonly employed isotopic signature and isotope effect derived from laboratory measurements reinforces the inherent sensitivity of NO_3^- isotopes to nitrification and denitrification. It also lends support to our interpretation that the observed chemostasis in NO_3^- export may be attributed to limited denitrification relative to NO_3^- transport and therefore a relatively homogeneous distribution of NO_3^-.

Therefore, through this simple modeling exercise, we outlined a possible way to couple NO_3^- isotopes with time-variant water age distributions, providing a proof-of-concept for its potential to unravel NO_3^- transport behaviors under transient conditions. In particular, the concise representation of flow path variations and water mixing by time-variant water age allows for the robust incorporation of important NO_3^- isotope fractionations to constrain the reactive transport of NO_3^-. A wide array of N cycling processes has been characterized for their isotope effects (Denk et al., 2017; Yu & Elliott, 2021). Incorporating these isotope effects into models of coupled soil moisture dynamics and N cycling (e.g., Porporato et al. (2003) and D'Odorico et al. (2003)) may provide important new insights to better understand water-N interactions. In this sense, the O isotopic systematics of nitrification is particularly important because it provides a direct link between the $\delta^{18}O$ of water, a commonly used water age tracer, and that of NO_3^-. If the O source contribution and the relevant isotope effects controlling the $\delta^{18}O$ of NO_3^- can be well understood and modeled at the watershed scale, the $\delta^{18}O$ of NO_3^- may be used as a "biogeochemical clock" to tag NO_3^- in individual water parcels for quantification of its reactive timescale. Future benchmark studies are needed to investigate the effects of varying isotope composition of reaction substrates (e.g., $\delta^{18}O$ of water), heterogeneity in isotope effects, and their variable expressions on modeling NO_3^- isotopes at the watershed scale.

6. Implications

The revealed young water preference and inverse storage effect at the tile-drain scale have important implications for modeling and managing water and N fluxes in intensively tile-drained agricultural watersheds. Most previous studies investigating the inverse storage effect have been conducted in small headwater watersheds (Benettin et al., 2017; Harman, 2015; Rodriguez et al., 2018). Although it remains largely unknown how water mixing and selection behaviors vary across spatial scales, extensive landscape modifications in tile-drained mesoscale watersheds in the Midwestern U.S. have been shown to create a homogenized system that responds to hydroclimatic forcings in a highly predictable way (Basu et al., 2011; Danesh-Yazdi et al., 2016). Moreover, at watershed scales, tile drains are themselves a preferential flow path that bypasses complex dispersion in the subsurface, resulting in water and solute delivery to the streams faster than they might naturally move within the soil matrix. Therefore, a strong young water preference and inverse storage effect is expected to be the norm in intensively tile-drained agricultural watersheds and should be used as a signature to test process representation in watershed-scale models.

From a management perspective, many on-farm agricultural practices influence subsurface drainage and nutrient losses to tile drains. For example, implementing no-till or reduced tillage on tile-drained fields has been shown to increase the likelihood of preferential flow to subsurface tile drains (Cullum, 2009). Tillage practices disrupt the continuity of macropore network, resulting in more torturous flow pathways for solute transport compared to no-tillage. While this tillage effect on phosphorus loss has been increasingly recognized and investigated (Williams et al., 2016), less attention has been paid to the increased risk of NO_3^- loss via preferential flow paths. This study indicates that surface-applied fertilizer N (including those incorporated or knifed into surface soil) is particularly prone to loss via preferential flows initiated in near-surface soil layers. As understanding the effects of agricultural management practices and changing climate on nutrient loadings in tile-drained landscapes is intensifying as a priority across the Midwestern U.S. (Danalatos et al., 2022), more research is needed to better understand the effects of tillage practices specifically and soil physical conditions in general on NO_3^- export from tile-drained fields.

By combining water age modeling with NO_3^- isotope analysis, this study provides evidence for the same-season loss of fertilizer N via tile drainage. In addition, labeled ^{15}N tracer studies have consistently demonstrate that in the Midwestern U.S. less than 40% of fertilizer N applied is recovered by the corn crop in the same year (Gardner & Drinkwater, 2009). While these different fates of fertilizer N (i.e., direct leaching and crop uptake) are well recognized by the N biogeochemistry research community, how to explicitly trace the fates of fertilizer N in watershed-scale models remains unexplored. This is mainly due to the lack of suitable tracer data at relevant scales, as well as to the commonly used "well-mixed" assumption when modeling soil N pools. As different sink pathways of fertilizer N represent vastly different residence timescales of N in a watershed, an advanced modeling approach that differentiates the fates and recycling pathways of fertilizer N at the watershed scale is vital in terms of quantifying the biogeochemical N legacy effect (Van Meter et al., 2018) and the long-term sustainability of agricultural watersheds. To that end, integrating NO_3^- isotope biogeochemistry with water age theory represents a promising avenue for future research to better model the source and sink strengths of N in hydrologic systems.

7. Conclusions

In this study, we combined SAS functions with NO_3^- isotope analysis to investigate storage, water mixing, and NO_3^- export regimes in a tile-drained corn-soybean rotation field. The calibration and evaluation of the SAS functions were based on a unique Cl data set measured at tile drain outlets that enables the modeling of both long-term storage variations and the transient variability of flow path activation during and between flow events. The SAS models were able to reproduce to a high goodness of fit the observed Cl dilution trend and revealed a strong young water preference during tile discharge generation. The use of a time-variant SAS function for tile discharge that follows the storage variations of the system was able to provide improved model performances in simulating short-term fluctuations in the Cl data set. More importantly, this time-variant parameterization generated unique water age dynamics that mechanically explain the observed variations in NO_3^- isotopes. Such linkages between water age and NO_3^- isotope dynamics highlight the promising potential of multi-tracer measurements to quantify coupled water and reactive solute transport in hydrologic systems. The revealed young water preference and inverse storage effect suggest a storage-dependent flow path activation mechanism, where rapid water and solute transport to tile drains is mediated by the activation of vertical preferential flow paths at near-surface soil horizons. Combining water age estimates with NO_3^- isotope analysis was able to delineate a clear picture of NO_3^- export at the tile-drain scale. The revealed chemostatic NO_3^- export regime and isotope dynamics suggest a lack of strong vertical contrast in NO_3^- concentration across the soil profile during the soybean year and the NGS of corn. The observed NO_3^- isotope variations following N fertilizer applications provide strong evidence for the direct loss of fertilizer-derived NO_3^- to the tile drains, which increased the variability of NO_3^- export during the GS of corn. However, further characterization of the NO_3^- export regime following fertilizer applications requires spatially extensive and high-frequency measurements to capture important "hot spots" and "hot moments" behaviors of tile NO_3^- loss. For the first time, NO_3^- isotopes were embedded into a water age-based transport model to assess their utility in constraining transient reactive NO_3^- transport. The results confirm the potential of NO_3^- isotopes to summarize the nonlinear interactions between hydrological and biogeochemical processes that control reactive NO_3^- transport. Further integration of water age modeling and NO_3^- isotope biogeochemistry is expected to significantly improve the knowledge and modeling of NO_3^- source and sink dynamics in complex hydrologic systems.

Appendix A: Calculation of NO_3^- Isotopologue Concentrations

Here we present the calculation procedure of NO_3^- isotopologue concentrations for the proposed NO_3^- transport modeling. Given the three stable isotopes of O (i.e., ^{16}O, ^{17}O, and ^{18}O), the molar concentrations of NO_3^- isotopologues are related to the total concentration of NO_3^- ($^{total}C$), which is directly measured, by Equation A1.

$$^{total}C = {}^{16}C + {}^{17}C + {}^{18}C \tag{A1}$$

where ^{16}C, ^{17}C, and ^{18}C are the molar concentrations of NO_3^- isotopologues $N^{16}O^{16}O^{16}O$, $N^{17}O^{16}O^{16}O$, and $N^{18}O^{16}O^{16}O$, respectively. We ignored the concentrations of multiply substituted isotopologues (e.g., $N^{18}O^{18}O^{16}O$) in Equation A1 due to their minute abundances. The atomic concentrations of the three O isotopes in NO_3^- can also be related to $^{total}C$ by accounting for the molar ratio between the NO_3^- molecule and the O atom (i.e., 1 mol of NO_3^- contains 3 mol of O atoms) (Equation A2).

$$[^{total}O] = 3 \times {}^{total}C = [^{16}O] + [^{17}O] + [^{18}O] \tag{A2}$$

Recall the definition of $\delta^{18}O\text{-}NO_3^-$:

$$\delta^{18}O = \left(\frac{[^{18}O]/[^{16}O]}{^{18}R_{VSMOW}} - 1\right) \times 1000 \tag{A3}$$

where $^{18}R_{VSMOW}$ refers to the ratio of ^{18}O and ^{16}O in the reference, Vienna standard mean ocean water (VSMOW). $^{18}R_{VSMOW} = 0.0020052$. Similarly, the $\delta^{17}O$ of NO_3^- is defined using the delta notation as:

$$\delta^{17}O = \left(\frac{[^{17}O]/[^{16}O]}{^{17}R_{VSMOW}} - 1\right) \times 1000 \tag{A4}$$

where $^{17}R_{VSMOW} = 0.0003799$. Although in this study we did not measure $\delta^{17}O$, the $\delta^{17}O$ of biologically produced NO_3^- (e.g., in contrast to photochemically produced NO_3^- such as atmospheric NO_3^-) is linked with the $\delta^{18}O$ of NO_3^- through the mass-dependent fractionation law (Yu & Elliott, 2018):

$$\delta^{17}O = 0.52 \times \delta^{18}O \tag{A5}$$

Equations A2–A5 can be combined and rearranged to solve for $[^{17}O]$ and $[^{18}O]$ using measured $^{total}C$ and $\delta^{18}O$:

$$[^{17}O] = \frac{3 \times {}^{total}C \times \left(\frac{0.52\times\delta^{18}O}{1000} + 1\right)^{17}R_{VSMOW}}{1 + \left(\frac{0.52\times\delta^{18}O}{1000} + 1\right)^{17}R_{VSMOW} + \left(\frac{\delta^{18}O}{1000} + 1\right)^{18}R_{VSMOW}} \tag{A6}$$

$$[^{18}O] = \frac{3 \times {}^{total}C \times \left(\frac{\delta^{18}O}{1000} + 1\right)^{18}R_{VSMOW}}{1 + \left(\frac{0.52\times\delta^{18}O}{1000} + 1\right)^{17}R_{VSMOW} + \left(\frac{\delta^{18}O}{1000} + 1\right)^{18}R_{VSMOW}} \tag{A7}$$

Because $N^{17}O^{16}O^{16}O$ and $N^{18}O^{16}O^{16}O$ are both singly substituted isotopologues, the atomic concentration of substituted O isotopes is equal to their molecular concentration:

$$^{17}C = [^{17}O] \tag{A8}$$

$$^{18}C = [^{18}O] \tag{A9}$$

Equations A1, A8, and A9 can then be combined to determine ^{16}C. This outlined procedure can be reversed to calculate $^{total}C$ and $\delta^{18}O$ from simulated ^{16}C and ^{18}C. A Matlab file for implementing the outlined procedure is available via Yu (2023b).

Data Availability Statement

The *trans*-SAS model code used for water age modeling is obtained from Benettin and Bertuzzo (2018a). Limited modification (i.e., Equation 12) and numerical operation of the *trans*-SAS model code are fully described in Section 3.5.3 of the present paper. The input climate, hydrological, and tracer data for running the SAS model and the model output for reproducing the presented results are available at Yu (2023a). The NO_3^- isotopologue transport model described in Section 5.3 are available at Yu (2023b).

Acknowledgments

This work was funded by the Illinois Nutrient Research and Education Council (Project 2021-4-360649-46 and 2014-5-360847-320), USDA-NIFA Hatch Project ILLU-875-983, and NSF (Grant 2110430). We are grateful to Naglis Subacius and Xiran Liu for assistance with laboratory analyses. We also thank Zewei Ma for discussion on an early version of this paper.

References

Allen, R. G., Pereira, L. S., Smith, M., Raes, D., & Wright, J. L. (2005). FAO-56 dual crop coefficient method for estimating evaporation from soil and application extensions. *Journal of Irrigation and Drainage Engineering*, *131*(1), 2–13. https://doi.org/10.1061/(asce)0733-9437(2005)131:1(2)

Andino, L. F., Gentry, L. E., & Fraterrigo, J. M. (2020). Closed depressions and soil phosphorus influence subsurface phosphorus losses in a tile-drained field in Illinois (Vol. *49*, No. (5), pp. 1273–1285).

Asadollahi, M., Stumpp, C., Rinaldo, A., & Benettin, P. (2020). Transport and water age dynamics in soils: A comparative study of spatially integrated and spatially explicit models. *Water Resources Research*, *56*(3), e2019WR025539. https://doi.org/10.1029/2019wr025539

Asano, Y., & Uchida, T. (2012). Flow path depth is the main controller of mean base flow transit times in a mountainous catchment. *Water Resources Research*, *48*(3), W03512. https://doi.org/10.1029/2011wr010906

Basu, N. B., Destouni, G., Jawitz, J. W., Thompson, S. E., Loukinova, N. V., Darracq, A., et al. (2010). Nutrient loads exported from managed catchments reveal emergent biogeochemical stationarity. *Geophysical Research Letters*, *37*(23), L23404. https://doi.org/10.1029/2010gl045168

Basu, N. B., Thompson, S. E., & Rao, P. S. C. (2011). Hydrologic and biogeochemical functioning of intensively managed catchments: A synthesis of top-down analyses. *Water Resources Research*, *47*(10), W00J15. https://doi.org/10.1029/2011wr010800

Batal, A., Dale, N., & Persia, M. (2011). Ngredient analysis table: 2012 ed. Feed-Stuffs.

Bauwe, A., Kahle, P., Tiemeyer, B., & Lennartz, B. (2020). Hydrology is the key factor for nitrogen export from tile-drained catchments under consistent land-management. *Environmental Research Letters*, *15*(9), 094050. https://doi.org/10.1088/1748-9326/aba580

Benettin, P., & Bertuzzo, E. (2018a). tran-SAS v1.0 [Code]. Zenodo. https://doi.org/10.5281/zenodo.1203600

Benettin, P., & Bertuzzo, E. (2018b). tran-SAS v1.0: A numerical model to compute catchment-scale hydrologic transport using StorAge Selection functions. *Geoscientific Model Development*, *11*(4), 1627–1639. https://doi.org/10.5194/gmd-11-1627-2018

Benettin, P., Fovet, O., & Li, L. (2020). Nitrate removal and young stream water fractions at the catchment scale. *Hydrological Processes*, *34*(12), 2725–2738. https://doi.org/10.1002/hyp.13781

Benettin, P., Rodriguez, N. B., Sprenger, M., Kim, M., Klaus, J., Harman, C. J., et al. (2022). Transit time estimation in catchments: Recent developments and future directions. *Water Resources Research*, *58*(11), e2022WR033096. https://doi.org/10.1029/2022wr033096

Benettin, P., Soulsby, C., Birkel, C., Tetzlaff, D., Botter, G., & Rinaldo, A. (2017). Using SAS functions and high-resolution isotope data to unravel travel time distributions in headwater catchments. *Water Resources Research*, *53*(3), 1864–1878. https://doi.org/10.1002/2016wr020117

Beven, K. (2006). A manifesto for the equifinality thesis. *Journal of Hydrology*, *320*(1–2), 18–36. https://doi.org/10.1016/j.jhydrol.2005.07.007

Bigeleisen, J., & Wolfsberg, M. (1957). Theoretical and experimental aspects of isotope effects in chemical kinetics. *Advances in Chemical Physics*, 15–76. https://doi.org/10.1002/9780470143476.ch2

Blann, K. L., Anderson, J. L., Sands, G. R., & Vondracek, B. (2009). Effects of agricultural drainage on aquatic ecosystems: A review. *Critical Reviews in Environmental Science and Technology*, *39*(11), 909–1001. https://doi.org/10.1080/10643380801977966

Böhlke, J. K. (2002). Groundwater recharge and agricultural contamination. *Hydrogeology Journal*, *10*(1), 153–179. https://doi.org/10.1007/s10040-001-0183-3

Botter, G., Bertuzzo, E., Bellin, A., & Rinaldo, A. (2005). On the Lagrangian formulations of reactive solute transport in the hydrologic response. *Water Resources Research*, *41*(4), W04008. https://doi.org/10.1029/2004wr003544

Botter, G., Bertuzzo, E., & Rinaldo, A. (2011). Catchment residence and travel time distributions: The master equation. *Geophysical Research Letters*, *38*(11), L11403. https://doi.org/10.1029/2011gl047666

Bowen, G. J., Putman, A., Brooks, J. R., Bowling, D. R., Oerter, E. J., & Good, S. P. (2018). Inferring the source of evaporated waters using stable H and O isotopes. *Oecologia*, *187*(4), 1025–1039. https://doi.org/10.1007/s00442-018-4192-5

Buchwald, C., & Casciotti, K. L. (2010). Oxygen isotopic fractionation and exchange during bacterial nitrite oxidation. *Limnology and Oceanography*, *55*(3), 1064–1074. https://doi.org/10.4319/lo.2010.55.3.1064

Cain, M. R., Woo, D. K., Kumar, P., Keefer, L., & Ward, A. S. (2022). Antecedent conditions control thresholds of tile-runoff generation and nitrogen export in intensively managed landscapes. *Water Resources Research*, *58*(2), e2021WR030507. https://doi.org/10.1029/2021wr030507

Casciotti, K. L. (2016). Nitrogen and oxygen isotopic studies of the marine nitrogen cycle. *Annual Review of Marine Science*, *8*(1), 379–407. https://doi.org/10.1146/annurev-marine-010213-135052

Casciotti, K. L., McIlvin, M., & Buchwald, C. (2010). Oxygen isotopic exchange and fractionation during bacterial ammonia oxidation. *Limnology and Oceanography*, *55*(2), 753–762. https://doi.org/10.4319/lo.2010.55.2.0753

Casciotti, K. L., Sigman, D. M., & Ward, B. B. (2003). Linking diversity and stable isotope fractionation in ammonia-oxidizing bacteria. *Geomicrobiology Journal*, *20*(4), 335–353. https://doi.org/10.1080/01490450303895

Chun, J. A., & Cooke, R. A. (2008). Calibrating Agridrain water level control structures using generalized weir and orifice equations. *Applied Engineering in Agriculture*, *24*(5), 595–602. https://doi.org/10.13031/2013.25274

Cullum, R. F. (2009). Macropore flow estimations under no-till and till systems. *Catena*, *78*(1), 87–91. https://doi.org/10.1016/j.catena.2009.03.004

Danalatos, G. J., Wolter, C., Archontoulis, S. V., & Castellano, M. J. (2022). Nitrate losses across 29 Iowa watersheds: Measuring long-term trends in the context of interannual variability. *Journal of Environmental Quality*, *51*(4), 708–718. https://doi.org/10.1002/jeq2.20349

Danesh-Yazdi, M., Foufoula-Georgiou, E., Karwan, D. L., & Botter, G. (2016). Inferring changes in water cycle dynamics of intensively managed landscapes via the theory of time-variant travel time distributions. *Water Resources Research*, *52*(10), 7593–7614. https://doi.org/10.1002/2016wr019091

David, M. B., Drinkwater, L. E., & McIsaac, G. F. (2010). Sources of nitrate yields in the Mississippi River Basin. *Journal of Environmental Quality*, *39*(5), 1657–1667. https://doi.org/10.2134/jeq2010.0115

David, M. B., Mitchell, C. A., Gentry, L. E., & Salemme, R. K. (2016). Chloride sources and losses in two tile-drained agricultural watersheds. *Journal of Environmental Quality*, *45*(1), 341–348. https://doi.org/10.2134/jeq2015.06.0302

Denk, T. R., Mohn, J., Decock, C., Lewicka-Szczebak, D., Harris, E., Butterbach-Bahl, K., et al. (2017). The nitrogen cycle: A review of isotope effects and isotope modeling approaches. *Soil Biology and Biochemistry*, *105*, 121–137. https://doi.org/10.1016/j.soilbio.2016.11.015

D'odorico, P., Laio, F., Porporato, A., & Rodriguez-Iturbe, I. (2003). Hydrologic controls on soil carbon and nitrogen cycles. II. A case study. *Advances in Water Resources*, *26*(1), 59–70. https://doi.org/10.1016/s0309-1708(02)00095-7

Fang, Y., Koba, K., Makabe, A., Takahashi, C., Zhu, W., Hayashi, T., et al. (2015). Microbial denitrification dominates nitrate losses from forest ecosystems. *Proceedings of the National Academy of Sciences of the United States of America*, *112*(5), 1470–1474. https://doi.org/10.1073/pnas.1416776112

Franzmeier, D. P. (1991). Estimation of hydraulic conductivity from effective porosity data for some Indiana soils. *Soil Science Society of America Journal*, *55*(6), 1801–1803. https://doi.org/10.2136/sssaj1991.03615995005500060050x

Gardner, J. B., & Drinkwater, L. E. (2009). The fate of nitrogen in grain cropping systems: A meta-analysis of ^{15}N field experiments. *Ecological Applications*, *19*(8), 2167–2184. https://doi.org/10.1890/08-1122.1

Godsey, S. E., Kirchner, J. W., & Clow, D. W. (2009). Concentration–discharge relationships reflect chemostatic characteristics of US catchments. *Hydrological Processes: International Journal*, *23*(13), 1844–1864. https://doi.org/10.1002/hyp.7315

Granger, J., Sigman, D. M., Prokopenko, M. G., Lehmann, M. F., & Tortell, P. D. (2006). A method for nitrite removal in nitrate N and O isotope analyses. *Limnology and Oceanography: Methods*, *4*(7), 205–212. https://doi.org/10.4319/lom.2006.4.205

Granger, J., & Wankel, S. D. (2016). Isotopic overprinting of nitrification on denitrification as a ubiquitous and unifying feature of environmental nitrogen cycling. *Proceedings of the National Academy of Sciences of the United States of America*, *113*(42), E6391–E6400. https://doi.org/10.1073/pnas.1601383113

Guan, K., Thompson, S. E., Harman, C. J., Basu, N. B., Rao, P. S. C., Sivapalan, M., et al. (2011). Spatiotemporal scaling of hydrological and agrochemical export dynamics in a tile-drained midwestern watershed. *Water Resources Research*, *47*(10), W00J02. https://doi.org/10.1029/2010wr009997

Harman, C. J. (2015). Time-variable transit time distributions and transport: Theory and application to storage-dependent transport of chloride in a watershed. *Water Resources Research*, *51*(1), 1–30. https://doi.org/10.1002/2014wr015707

Houlton, B. Z., & Bai, E. (2009). Imprint of denitrifying bacteria on the global terrestrial biosphere. *Proceedings of the National Academy of Sciences of the United States of America*, *106*(51), 21713–21716. https://doi.org/10.1073/pnas.0912111106

Houlton, B. Z., Sigman, D. M., & Hedin, L. O. (2006). Isotopic evidence for large gaseous nitrogen losses from tropical rainforests. *Proceedings of the National Academy of Sciences of the United States of America*, *103*(23), 8745–8750. https://doi.org/10.1073/pnas.0510185103

Hrachowitz, M., Benettin, P., Van Breukelen, B. M., Fovet, O., Howden, N. J., Ruiz, L., et al. (2016). Transit times—The link between hydrology and water quality at the catchment scale. *Wiley Interdisciplinary Reviews: Water*, *3*(5), 629–657. https://doi.org/10.1002/wat2.1155

Hrachowitz, M., Fovet, O., Ruiz, L., & Savenije, H. H. (2015). Transit time distributions, legacy contamination and variability in biogeochemical 1/fα scaling: How are hydrological response dynamics linked to water quality at the catchment scale? *Hydrological Processes*, *29*(25), 5241–5256. https://doi.org/10.1002/hyp.10546

Hrachowitz, M., Savenije, H., Bogaard, T. A., Tetzlaff, D., & Soulsby, C. (2013). What can flux tracking teach us about water age distribution patterns and their temporal dynamics? *Hydrology and Earth System Sciences*, *17*(2), 533–564. https://doi.org/10.5194/hess-17-533-2013

Illinois Agronomy Handbook. (2014). Retrieved from https://extension.illinois.edu/global/agronomy-handbook

Jiang, Y., & Somers, G. (2009). Modeling effects of nitrate from non-point sources on groundwater quality in an agricultural watershed in Prince Edward Island, Canada. *Hydrogeology Journal*, *17*(3), 707–724. https://doi.org/10.1007/s10040-008-0390-2

Kaandorp, V. P., De Louw, P. G. B., Van der Velde, Y., & Broers, H. P. (2018). Transient groundwater travel time distributions and age-ranked storage-discharge relationships of three lowland catchments. *Water Resources Research*, *54*(7), 4519–4536. https://doi.org/10.1029/2017wr022461

Kaushal, S. S., Groffman, P. M., Band, L. E., Elliott, E. M., Shields, C. A., & Kendall, C. (2011). Tracking nonpoint source nitrogen pollution in human-impacted watersheds. *Environmental Science & Technology*, *45*(19), 8225–8232. https://doi.org/10.1021/es200779e

Kendall, C., Elliott, E. M., & Wankel, S. D. (2007). Tracing anthropogenic inputs of nitrogen to ecosystems. *Stable Isotopes in Ecology and Environmental Science*, *2*(1), 375–449. https://doi.org/10.1002/9780470691854.ch12

Kim, M., Pangle, L. A., Cardoso, C., Lora, M., Volkmann, T. H., Wang, Y., et al. (2016). Transit time distributions and StorAge Selection functions in a sloping soil lysimeter with time-varying flow paths: Direct observation of internal and external transport variability. *Water Resources Research*, *52*(9), 7105–7129. https://doi.org/10.1002/2016wr018620

Kirchner, J. W. (2009). Catchments as simple dynamical systems: Catchment characterization, rainfall-runoff modeling, and doing hydrology backward. *Water Resources Research*, *45*(2), W02429. https://doi.org/10.1029/2008wr006912

Kirchner, J. W., Tetzlaff, D., & Soulsby, C. (2010). Comparing chloride and water isotopes as hydrological tracers in two Scottish catchments. *Hydrological Processes*, *24*(12), 1631–1645. https://doi.org/10.1002/hyp.7676

Klaus, J., Zehe, E., Elsner, M., Külls, C., & McDonnell, J. J. (2013). Macropore flow of old water revisited: Experimental insights from a tile-drained hillslope. *Hydrology and Earth System Sciences*, *17*(1), 103–118. https://doi.org/10.5194/hess-17-103-2013

Kling, H., Fuchs, M., & Paulin, M. (2012). Runoff conditions in the upper Danube basin under an ensemble of climate change scenarios. *Journal of Hydrology*, *424*, 264–277. https://doi.org/10.1016/j.jhydrol.2012.01.011

Kumar, R., Heße, F., Rao, P. S. C., Musolff, A., Jawitz, J. W., Sarrazin, F., et al. (2020). Strong hydroclimatic controls on vulnerability to subsurface nitrate contamination across Europe. *Nature Communications*, *11*(1), 6302. https://doi.org/10.1038/s41467-020-19955-8

Li, L., Sullivan, P. L., Benettin, P., Cirpka, O. A., Bishop, K., Brantley, S. L., et al. (2021). Toward catchment hydro-biogeochemical theories. *Wiley Interdisciplinary Reviews: Water*, *8*(1), e1495. https://doi.org/10.1002/wat2.1495

Liu, W., Youssef, M. A., Birgand, F. P., Chescheir, G. M., Tian, S., & Maxwell, B. M. (2020). Processes and mechanisms controlling nitrate dynamics in an artificially drained field: Insights from high-frequency water quality measurements. *Agricultural Water Management*, *232*, 106032. https://doi.org/10.1016/j.agwat.2020.106032

Ma, Z., Guan, K., Peng, B., Sivapalan, M., Li, L., Pan, M., et al. (2023). Agricultural nitrate export patterns shaped by crop rotation and tile drainage. *Water Research*, *229*, 119468. https://doi.org/10.1016/j.watres.2022.119468

Mariotti, A., Germon, J. C., Hubert, P., Kaiser, P., Letolle, R., Tardieux, A., & Tardieux, P. (1981). Experimental determination of nitrogen kinetic isotope fractionation: Some principles; illustration for the denitrification and nitrification processes. *Plant and Soil*, *62*(3), 413–430. https://doi.org/10.1007/bf02374138

McGuire, K. J., & McDonnell, J. J. (2006). A review and evaluation of catchment transit time modeling. *Journal of Hydrology*, *330*(3–4), 543–563. https://doi.org/10.1016/j.jhydrol.2006.04.020

Mnich, M. E., & Houlton, B. Z. (2016). Evidence for a uniformly small isotope effect of nitrogen leaching loss: Results from disturbed ecosystems in seasonally dry climates. *Oecologia*, *181*(2), 323–333. https://doi.org/10.1007/s00442-015-3433-0

Musolff, A., Fleckenstein, J. H., Rao, P. S. C., & Jawitz, J. W. (2017). Emergent archetype patterns of coupled hydrologic and biogeochemical responses in catchments. *Geophysical Research Letters*, *44*(9), 4143–4151. https://doi.org/10.1002/2017gl072630

Musolff, A., Schmidt, C., Selle, B., & Fleckenstein, J. H. (2015). Catchment controls on solute export. *Advances in Water Resources*, *86*, 133–146. https://doi.org/10.1016/j.advwatres.2015.09.026

NADP. (2023). National atmospheric deposition program for Bonville, Illinois (site ID IL11). Retrieved from https://www.usgs.gov/mission-areas/water-resources/science/national-atmospheric-deposition-program-nadp

NOAA. (2022). Historical daily conditions of Tuscola, IL (USC00118684). Retrieved from https://www.ncei.noaa.gov/maps-and-geospatial-products

Pangle, L. A., Kim, M., Cardoso, C., Lora, M., Meira Neto, A. A., Volkmann, T. H., et al. (2017). The mechanistic basis for storage-dependent age distributions of water discharged from an experimental hillslope. *Water Resources Research*, *53*(4), 2733–2754. https://doi.org/10.1002/2016wr019901

Porporato, A., D'odorico, P., Laio, F., & Rodriguez-Iturbe, I. (2003). Hydrologic controls on soil carbon and nitrogen cycles. I. Modeling scheme. *Advances in Water Resources*, *26*(1), 45–58. https://doi.org/10.1016/s0309-1708(02)00094-5

Porter, L. K., Kemper, W. D., Jackson, R. D., & Stewart, B. A. (1960). Chloride diffusion in soils as influenced by moisture content. *Soil Science Society of America Journal*, *24*(6), 460–463. https://doi.org/10.2136/sssaj1960.03615995002400060014x

Queloz, P., Carraro, L., Benettin, P., Botter, G., Rinaldo, A., & Bertuzzo, E. (2015). Transport of fluorobenzoate tracers in a vegetated hydrologic control volume: 2. Theoretical inferences and modeling. *Water Resources Research*, *51*(4), 2793–2806. https://doi.org/10.1002/2014wr016508

Rinaldo, A., Benettin, P., Harman, C. J., Hrachowitz, M., McGuire, K. J., Van Der Velde, Y., et al. (2015). Storage selection functions: A coherent framework for quantifying how catchments store and release water and solutes. *Water Resources Research*, *51*(6), 4840–4847. https://doi.org/10.1002/2015wr017273

Rinaldo, A., & Marani, A. (1987). Basin scale model of solute transport. *Water Resources Research*, *23*(11), 2107–2118. https://doi.org/10.1029/wr023i011p02107

Rodriguez, N. B., & Klaus, J. (2019). Catchment travel times from composite StorAge Selection functions representing the superposition of streamflow generation processes. *Water Resources Research*, *55*(11), 9292–9314. https://doi.org/10.1029/2019wr024973

Rodriguez, N. B., McGuire, K. J., & Klaus, J. (2018). Time-varying storage–water age relationships in a catchment with a mediterranean climate. *Water Resources Research*, *54*(6), 3988–4008. https://doi.org/10.1029/2017wr021964

Rose, L. A., & Karwan, D. L. (2021). Stormflow concentration–discharge dynamics of suspended sediment and dissolved phosphorus in an agricultural watershed. *Hydrological Processes*, *35*(12), e14455. https://doi.org/10.1002/hyp.14455

Sebestyen, S. D., Ross, D. S., Shanley, J. B., Elliott, E. M., Kendall, C., Campbell, J. L., et al. (2019). Unprocessed atmospheric nitrate in waters of the northern forest region in the US and Canada. *Environmental Science & Technology*, *53*(7), 3620–3633. https://doi.org/10.1021/acs.est.9b01276

Seibert, J., Grabs, T., Köhler, S., Laudon, H., Winterdahl, M., & Bishop, K. (2009). Linking soil-and stream-water chemistry based on a Riparian flow-concentration integration model. *Hydrology and Earth System Sciences*, *13*(12), 2287–2297. https://doi.org/10.5194/hess-13-2287-2009

Stone, W. W., & Wilson, J. T. (2006). Preferential flow estimates to an agricultural tile drain with implications for glyphosate transport. *Journal of Environmental Quality*, *35*(5), 1825–1835. https://doi.org/10.2134/jeq2006.0068

Thompson, S. E., Basu, N. B., Lascurain, J., Jr., Aubeneau, A., & Rao, P. S. C. (2011). Relative dominance of hydrologic versus biogeochemical factors on solute export across impact gradients. *Water Resources Research*, *47*(10), W00J05. https://doi.org/10.1029/2010wr009605

USDA-NRCS. (2016). Gridded soil survey geographic (gSSURGO) database for Douglas county, Illinois. Retrieved from https://gdg.sc.egov.usda.gov/

USGS. (2023). Water data for the nation. Daily discharge data of Embarras River near Camargo, IL (03343400). Retrieved from https://waterdata.usgs.gov/monitoring-location/03343400/#parameterCode=00065&period=P7D

Van der Velde, Y., De Rooij, G. H., Rozemeijer, J. C., Van Geer, F. C., & Broers, H. P. (2010). Nitrate response of a lowland catchment: On the relation between stream concentration and travel time distribution dynamics. *Water Resources Research*, *46*(11), W00J05. https://doi.org/10.1029/2010wr009105

Van der Velde, Y., De Rooij, G. H., & Torfs, P. J. J. F. (2009). Catchment-scale non-linear groundwater-surface water interactions in densely drained lowland catchments. *Hydrology and Earth System Sciences*, *13*(10), 1867–1885. https://doi.org/10.5194/hess-13-1867-2009

van der Velde, Y., Rozemeijer, J. C., de Rooij, G. H., van Geer, F. C., & Broers, H. P. (2010). Field-scale measurements for separation of catchment discharge into flow route contributions. *Vadose Zone Journal*, *9*(1), 25–35. https://doi.org/10.2136/vzj2008.0141

Van Der Velde, Y., Torfs, P. J. J. F., Van Der Zee, S. E. A. T. M., & Uijlenhoet, R. (2012). Quantifying catchment-scale mixing and its effect on time-varying travel time distributions. *Water Resources Research*, *48*(6), W06536. https://doi.org/10.1029/2011wr011310

Van Meter, K. J., Van Cappellen, P., & Basu, N. B. (2018). Legacy nitrogen may prevent achievement of water quality goals in the Gulf of Mexico. *Science*, *360*(6387), 427–430. https://doi.org/10.1126/science.aar4462

Vidon, P., & Cuadra, P. E. (2010). Impact of precipitation characteristics on soil hydrology in tile-drained landscapes. *Hydrological Processes*, *24*(13), 1821–1833. https://doi.org/10.1002/hyp.7627

Weigand, M. A., Foriel, J., Barnett, B., Oleynik, S., & Sigman, D. M. (2016). Updates to instrumentation and protocols for isotopic analysis of nitrate by the denitrifier method. *Rapid Communications in Mass Spectrometry*, *30*(12), 1365–1383. https://doi.org/10.1002/rcm.7570

Williams, M. R., King, K. W., Ford, W., Buda, A. R., & Kennedy, C. D. (2016). Effect of tillage on macropore flow and phosphorus transport to tile drains. *Water Resources Research*, *52*(4), 2868–2882. https://doi.org/10.1002/2015wr017650

Williams, M. R., & McAfee, S. J. (2021). Water storage, mixing, and fluxes in tile-drained agricultural fields inferred from stable water isotopes. *Journal of Hydrology*, *599*, 126347. https://doi.org/10.1016/j.jhydrol.2021.126347

Wilusz, D. C., Harman, C. J., Ball, W. P., Maxwell, R. M., & Buda, A. R. (2020). Using particle tracking to understand flow paths, age distributions, and the paradoxical origins of the inverse storage effect in an experimental catchment. *Water Resources Research*, *56*(4), e2019WR025140. https://doi.org/10.1029/2019wr025140

Woo, D. K., & Kumar, P. (2019). Impacts of subsurface tile drainage on age—Concentration dynamics of inorganic nitrogen in soil. *Water Resources Research*, *55*(2), 1470–1489. https://doi.org/10.1029/2018wr024139

Yang, J., Heidbüchel, I., Musolff, A., Reinstorf, F., & Fleckenstein, J. H. (2018). Exploring the dynamics of transit times and subsurface mixing in a small agricultural catchment. *Water Resources Research*, *54*(3), 2317–2335. https://doi.org/10.1002/2017wr021896

Yi, Q., Chen, Q., Hu, L., & Shi, W. (2017). Tracking nitrogen sources, transformation, and transport at a basin scale with complex plain river networks. *Environmental Science & Technology*, *51*(10), 5396–5403. https://doi.org/10.1021/acs.est.6b06278

Yu, Z. (2023a). Linking water age, nitrate export regime, and nitrate isotope biogeochemistry in a tile-drained agricultural field [Dataset]. Zenodo. https://doi.org/10.5281/zenodo.7761579

Yu, Z. (2023b). Linking water age, nitrate export regime, and nitrate isotope biogeochemistry in a tile-drained agricultural field: The nitrate isotopologue transport model [Code]. Zenodo. https://doi.org/10.5281/zenodo.7761585

Yu, Z., & Elliott, E. M. (2018). Probing soil nitrification and nitrate consumption using Δ^{17}O of soil nitrate. *Soil Biology and Biochemistry*, *127*, 187–199. https://doi.org/10.1016/j.soilbio.2018.09.029

Yu, Z., & Elliott, E. M. (2021). Nitrogen isotopic fractionations during nitric oxide production in an agricultural soil. *Biogeosciences*, *18*(3), 805–829. https://doi.org/10.5194/bg-18-805-2021

References From the Supporting Information

Brauer, C. C., Teuling, A. J., Torfs, P. J. J. F., & Uijlenhoet, R. (2013). Investigating storage-discharge relations in a lowland catchment using hydrograph fitting, recession analysis, and soil moisture data. *Water Resources Research*, *49*(7), 4257–4264. https://doi.org/10.1002/wrcr.20320

Brutsaert, W., & Nieber, J. L. (1977). Regionalized drought flow hydrographs from a mature glaciated plateau. *Water Resources Research*, *13*(3), 637–643. https://doi.org/10.1029/wr013i003p00637

Fritton, D. D., Kirkham, D., & Shaw, R. H. (1967). Soil water and chloride redistribution under various evaporation potentials. *Soil Science Society of America Journal*, *31*(5), 599–603. https://doi.org/10.2136/sssaj1967.03615995003100050002x

Rupp, D. E., & Selker, J. S. (2006a). Information, artifacts, and noise in dQ/dt− Q recession analysis. *Advances in Water Resources*, *29*(2), 154–160. https://doi.org/10.1016/j.advwatres.2005.03.019

Rupp, D. E., & Selker, J. S. (2006b). On the use of the Boussinesq equation for interpreting recession hydrographs from sloping aquifers. *Water Resources Research*, *42*(12), W12421. https://doi.org/10.1029/2006wr005080

Rupp, D. E., Owens, J. M., Warren, K. L., & Selker, J. S. (2004). Analytical methods for estimating saturated hydraulic conductivity in a tile-drained field. *Journal of Hydrology*, *289*(1–4), 111–127. https://doi.org/10.1016/j.jhydrol.2003.11.004

Teuling, A. J., Lehner, I., Kirchner, J. W., & Seneviratne, S. I. (2010). Catchments as simple dynamical systems: Experience from a Swiss prealpine catchment. *Water Resources Research*, *46*(10), W12421. https://doi.org/10.1029/2009wr008777